

**Light hadron spectroscopy with  $O(a)$  improved dynamical fermions**C. R. Allton,<sup>1</sup> S. P. Booth,<sup>2</sup> K. C. Bowler,<sup>3</sup> M. Foster,<sup>4</sup> J. Garden,<sup>3</sup> A. C. Irving,<sup>4</sup> R. D. Kenway,<sup>3</sup> C. Michael,<sup>4</sup> J. Peisa,<sup>4</sup> S. M. Pickles,<sup>3</sup> J. C. Sexton,<sup>5</sup> Z. Sroczynski,<sup>3</sup> M. Talevi,<sup>3</sup> and H. Wittig<sup>6</sup>

(UKQCD Collaboration)

<sup>1</sup>*Department of Physics, University of Wales, Singleton Park, Swansea SA2 8PP, United Kingdom*<sup>2</sup>*Edinburgh Parallel Computing Centre, University of Edinburgh, Edinburgh EH9 3JZ, Scotland*<sup>3</sup>*Department of Physics & Astronomy, University of Edinburgh, Edinburgh EH9 3JZ, Scotland*<sup>4</sup>*Division of Theoretical Physics, Department of Mathematical Sciences, University of Liverpool, Liverpool L69 3BX, United Kingdom*<sup>5</sup>*School of Mathematics, Trinity College, Dublin 2, Ireland**and Hitachi Dublin Laboratory, Dublin 2, Ireland*<sup>6</sup>*Theoretical Physics, University of Oxford, Oxford OX1 3NP, United Kingdom*

(Received 17 August 1998; published 7 July 1999)

We present the first results for the static quark potential and the light hadron spectrum using dynamical fermions at  $\beta=5.2$  using an  $O(a)$  improved Wilson fermion action together with the standard Wilson plaquette action for the gauge part. Sea quark masses were chosen such that the pseudoscalar-vector mass ratio,  $m_{PS}/m_V$ , varies from 0.86 to 0.67. Finite-size effects are studied by using three different volumes  $8^3 \times 24$ ,  $12^3 \times 24$ , and  $16^3 \times 24$ . Comparing our results to previous ones obtained using the quenched approximation, we find evidence for sea quark effects in quantities such as the static quark potential and vector-pseudoscalar hyperfine splitting. [S0556-2821(99)00613-X]

PACS number(s): 12.38.Gc, 12.40.Yx

**I. INTRODUCTION**

Recent years have seen a lot of progress in understanding the spectrum and decays of hadrons using numerical simulations of lattice QCD (for recent reviews, see [1–3]). While much effort has been invested in controlling systematic errors such as finite-size effects and lattice artifacts, the inclusion of quark loops in the stochastic evaluation of the Feynman path integral still presents a major challenge. Therefore, most simulations rely on the quenched approximation for which the systematic errors incurred by neglecting dynamical quark effects cannot be assessed. However, recent progress in the development of efficient algorithms [4] and increased computer power have greatly increased the prospects for simulations with dynamical quarks. Several groups have published results for hadronic quantities in the light quark sector and the static quark potential from dynamical simulations [5–12]. At the same time it has been demonstrated that leading lattice artifacts of order  $a$  in physical observables can be eliminated through the nonperturbative implementation of the Symanzik improvement program [13,14]. The nonperturbatively  $O(a)$  improved Wilson action has been determined in the quenched approximation [15,16], and first results have also been reported for  $n_f=2$  flavors of dynamical quarks [17]. This enables one to study the effects of the inclusion of dynamical quarks while having better control over discretization errors.

In this work we report on calculations of the light hadron spectrum using two flavors of  $O(a)$  improved dynamical Wilson quarks at  $\beta=5.2$ . For the improvement (clover) coefficient, we have used  $c_{sw}=1.76$ , a preliminary estimate kindly supplied by the ALPHA Collaboration prior to the final result  $c_{sw}=2.017$  at  $\beta=5.2$ , presented in [17]. The

main aim of this study is to understand the qualitative features of dynamical simulations with improved fermions, such as the sea quark mass dependence of observables, finite-volume effects, and estimates of autocorrelation times. The complete removal of  $O(a)$  lattice artifacts is therefore not our highest priority in this work. Results for the hadron spectrum obtained with the “correct” values of  $c_{sw}$  will be published elsewhere [18].

The plan for the remainder of this paper is as follows. In Sec. II we describe the details of our simulation, including the implementation of the algorithm and the analysis of autocorrelations. Section III contains our results for the static quark potential. The results for the light hadron spectrum and discussions of finite-volume and sea quark effects are presented in Sec. IV. Section V contains our conclusions. Finally, in the Appendix A we list our results for hadron masses on all lattice sizes and parameter values.

**II. SIMULATION**

In this section we fix our notation, describe the details of the implementation of the generalized hybrid Monte Carlo (GHMC) algorithm [19] on the Cray T3E, and give an overview of the simulation parameters used in our calculation. We end this section with a discussion of autocorrelations.

**A. Lattice action**

The lattice action can be split into a pure gauge part  $S_G$  and a fermionic part  $S_F$ :

$$S[U, \bar{\psi}, \psi] = S_G[U] + S_F[U, \bar{\psi}, \psi], \quad (1)$$

where

$$S_G[U] = \beta \sum_P \left( 1 - \frac{1}{3} \text{Re Tr } U_P \right) \quad (2)$$

is the Wilson plaquette action and  $S_F$  is defined by

$$S_F[U, \bar{\psi}, \psi] = S_F^W[U, \bar{\psi}, \psi] - c_{sw} \frac{i\kappa}{2} \sum_{x, \mu, \nu} \bar{\psi}(x) \sigma_{\mu\nu} F_{\mu\nu}(x) \psi(x). \quad (3)$$

Here  $S_F^W$  is the standard Wilson action and  $c_{sw}$  denotes the improvement coefficient multiplying the Sheikholeslami-Wohlert term [20]. The bare parameters of the theory are the gauge coupling  $\beta \equiv 6/g_0^2$  and the hopping parameter  $\kappa$ . Here we work with a doublet of degenerate dynamical Wilson quarks, and hence gauge configurations are characterized by the set of parameters  $(\beta, \kappa; c_{sw})$ . For a description of the GHMC algorithm, it is useful to rewrite the fermionic part of the action in terms of a complex, bosonic pseudofermion field  $\phi$ . In matrix notation we have

$$S_F = \phi^\dagger (M^\dagger M)^{-1} \phi - 2 \sum_{\text{even sites}} \ln \det A_{xx}. \quad (4)$$

The odd-even preconditioned fermion matrix  $M$  is given by

$$M_{xy} = A_{xx} - \kappa^2 D_{xz} A_{zz}^{-1} D_{zy}, \quad (5)$$

where  $D$  is the Wilson-Dirac matrix and  $A$  denotes the matrix for the Sheikholeslami-Wohlert term.

## B. Implementation of the GHMC algorithm

The main limitation of the performance of the Cray T3E is the memory bandwidth. The increased complexity of the memory system and the fact that the processors support multiple instruction issue leads to a loss of performance even for highly optimized FORTRAN codes. We have therefore chosen to write key routines in ASSEMBLER, while using FORTRAN 90 for less CPU-intensive parts. Less than 25% of the required run time is spent executing FORTRAN code.

Using 32-bit instead of 64-bit precision to represent the fields increases the speed by a factor 1.7. However, this gain has to be weighed against the degradation of the acceptance rate, reversibility, and the accuracy in the evaluation of the (global) energy difference required in the Metropolis accept-reject step. The last issue has been addressed by evaluating energy differences site by site and performing the subsequent summation in higher precision.

The inversion of the fermion matrix was performed using the stabilized biconjugate gradient (BICGSTAB) algorithm with odd-even preconditioning [21]. The gain compared to using the ordinary conjugate gradient algorithm was 40%. Further algorithmic improvements applied in this simulation are described in [22].

The version of the Cray T3E used in this work consisted of 96 processors, each capable of 900 MFlops peak speed. Using all our algorithmic improvements and exploiting the architectural features of the T3E, we typically achieve sustained speeds of 25–30 GFlops on such a configuration.

We now describe the integration schemes used in the molecular dynamics part of the GHMC algorithm. As usual, one introduces a set of conjugate momenta  $P$  for the gauge fields  $U$ . The HMC Hamiltonian is then defined as

$$\mathcal{H} = T[P] + S_G[U] + S_F[U, \phi^\dagger, \phi], \quad (6)$$

where  $T[P]$  is the kinetic energy and we have written  $S_F$  in terms of the pseudofermion fields  $\phi$  and  $\phi^\dagger$ . Here  $T[P]$  is related to the evolution operator  $\mathcal{T}$  in molecular dynamics time  $\tau$ , so that for any given set  $U$  and  $P$  of gauge fields and conjugate momenta, respectively [23],

$$\mathcal{T} = \begin{pmatrix} T_P \\ T_U \end{pmatrix}: \begin{pmatrix} U(\tau) \\ P(\tau) \end{pmatrix} \rightarrow \begin{pmatrix} U(\tau + d\tau) \\ P(\tau + d\tau) \end{pmatrix}, \quad (7)$$

where  $d\tau$  denotes a finite interval in simulation time. The operators  $T_P$  and  $T_U$  are defined by

$$T_P(d\tau): U \rightarrow e^{id\tau P} U, \\ T_U(d\tau): P \rightarrow P - id\tau \frac{\partial}{\partial U} (S_G + S_F). \quad (8)$$

Since  $\mathcal{T}$  represents a numerical integration of the equations of motion, it does not conserve  $\mathcal{H}$ , but introduces an error  $\Delta\mathcal{H}$ . For a single application of  $\mathcal{T}$ , this error is expected to grow as a power of the time step  $d\tau$  [24,25]:

$$\Delta\mathcal{H} \propto (d\tau)^q. \quad (9)$$

Verification of this relation for a given integration scheme provides a check on the correct implementation of the equations of motion. We have compared three integration schemes defined by

$$T_1 = T_P(d\tau) T_U(d\tau), \quad (10)$$

$$T_2 = T_P\left(\frac{d\tau}{2}\right) T_U(d\tau) T_P\left(\frac{d\tau}{2}\right), \quad (11)$$

$$T_3 = T_P\left(\frac{a}{2} d\tau\right) T_U(a d\tau) T_P\left(\frac{a+b}{2} d\tau\right) T_U(b d\tau) \\ \times T_P\left(\frac{a+b}{2} d\tau\right) T_U(a d\tau) T_P\left(\frac{a}{2} d\tau\right), \quad (12)$$

where  $a = 1/(2 - 2^{1/3})$  and  $b = -2^{1/3}/(2 - 2^{1/3})$ . Note that  $T_2$  is the standard leapfrog integration scheme. One expects that  $T_1$ ,  $T_2$ , and  $T_3$  cause  $\Delta\mathcal{H}$  to vary as  $(d\tau)^2$ ,  $(d\tau)^3$ , and  $(d\tau)^5$ , respectively. This can be compared to the values of  $q$  obtained from the slope of  $\ln \Delta\mathcal{H}$  as a function of  $\ln(d\tau)$ . Such a comparison is shown in Table I. The numerically determined values of  $q$  agree well with the expected behavior of  $\Delta\mathcal{H}$  for the three integration schemes, and thus we conclude that the integration of the equations of motion has been implemented correctly. In our production runs we have chosen an integration scheme which, like  $T_2$ , is exact up to order  $(d\tau)^3$ . To this end we define the operators

TABLE I. Leading variation of  $\Delta\mathcal{H}$  for the three integration schemes considered and measured values of  $q$ .

Scheme	$(d\tau)^q$	$q$
$T_1$	$(d\tau)^2$	1.982(4)
$T_2$	$(d\tau)^3$	3.053(2)
$T_3$	$(d\tau)^5$	5.056(6)

$$T_G(d\tau): \quad P \rightarrow P - i d\tau \frac{\partial}{\partial U} S_G,$$

$$T_F(d\tau): \quad P \rightarrow P - i d\tau \frac{\partial}{\partial U} S_F, \quad (13)$$

and consider the generalized leapfrog integration scheme

$$T(d\tau) = T_F\left(\frac{d\tau}{2}\right) \left[ T_G\left(\frac{d\tau}{2n}\right) T_P\left(\frac{d\tau}{n}\right) T_G\left(\frac{d\tau}{2n}\right) \right]^n T_F\left(\frac{d\tau}{2}\right). \quad (14)$$

This particular scheme allows for a more efficient evaluation of the derivative of  $S_G + S_F$  with respect to the gauge field. It reduces to the simple leapfrog scheme for  $n=1$ . In practice, we have used  $n=1$  or 2.

Finally, we note that although the generalized hybrid Monte Carlo algorithm had been implemented, we have used standard hybrid Monte Carlo algorithm in all production runs.

### C. Simulation parameters

Our simulations have been performed at  $\beta=5.2$ . In order to be able to study consistently finite-volume effects and the dependence on the dynamical quark mass, we have used  $c_{\text{sw}}=1.76$  in all calculations described in this paper. The standard lattice size in this simulation was  $12^3 \times 24$  and was chosen such as to guarantee a spatial volume in physical units of more than  $(1 \text{ fm})^3$ . Smaller and larger lattices of size  $8^3 \times 24$  and  $16^3 \times 24$  were used to monitor finite-size effects.

In order to distinguish the bare quark mass used in the generation of dynamical configurations from that used to compute quark propagators for hadronic observables, we introduce the notation  $\kappa^{\text{sea}}$  to denote the hopping parameter of the doublet of dynamical quarks, while reserving  $\kappa^{\text{val}}$  for the valence quarks. In order to study the dependence of observables on the sea quark mass, gauge configurations have been generated at several values of  $\kappa^{\text{sea}}$ . In Table II we list lattice sizes, the values of  $\kappa^{\text{sea}}$  and  $\kappa^{\text{val}}$ , and the number of configurations.

Quark propagators were calculated for every combination of  $(\kappa^{\text{sea}}, \kappa^{\text{val}})$  and combined to form hadronic two-point correlation functions. In order to increase the projection onto the ground state, the quark propagators used to form hadronic two-point functions have been “fuzzed” at the source and/or sink according to the prescription defined in [26]. Statistical errors of observables have been estimated using the bootstrap procedure described in [27] using 250 bootstrap samples.

### D. Autocorrelations

The determination of autocorrelation times is important in order to achieve small statistical correlations among the ensemble of configurations and to eliminate the effects of insufficient thermalization.

The autocovariance of an observable  $\Omega$  is defined as [28]

$$\Gamma_\Omega(t) = \langle (\Omega_s - \langle \Omega \rangle) (\Omega_{s+t} - \langle \Omega \rangle) \rangle, \quad (15)$$

where the subscripts on  $\Omega$  label the values obtained on successive configurations. In practice, the expectation value  $\langle \dots \rangle$  is replaced by the ensemble average over a finite number of configurations. We define the autocorrelation function of  $\Omega$  by

$$\rho_\Omega(t) = \Gamma_\Omega(t) / \Gamma_\Omega(0), \quad (16)$$

and from the large- $t$  behavior of  $\rho_\Omega$  one obtains the exponential autocorrelation time  $\tau^{\text{exp}}$ :

$$\rho_\Omega(t) \propto e^{-t/\tau^{\text{exp}}}, \quad t \rightarrow \infty. \quad (17)$$

TABLE II. Summary of simulation parameters and statistics for the computation of hadronic observables.

$L^3 \times T$	$\beta$	$c_{\text{sw}}$	No. conf.	$\kappa^{\text{sea}}$	$\kappa^{\text{val}}$			
$8^3 \times 24$	5.2	1.76	78	0.1370	0.1370	0.1380	0.1390	0.1395
			100	0.1380	0.1370	0.1380	0.1390	0.1395
			100	0.1390	0.1370	0.1380	0.1390	0.1395
			60	0.1395	0.1370	0.1380	0.1390	0.1395
			151	0.1370	0.1370	0.1380	0.1390	0.1395
$12^3 \times 24$	5.2	1.76	151	0.1380	0.1370	0.1380	0.1390	0.1395
			151	0.1390	0.1370	0.1380	0.1390	0.1395
			121	0.1395	0.1370	0.1380	0.1390	0.1395
			98	0.1398		0.1380	0.1390	0.1395
			90	0.1390			0.1390	0.1395
$16^3 \times 24$	5.2	1.76	100	0.1395			0.1390	0.1395
			69	0.1398			0.1390	0.1395
								0.1398

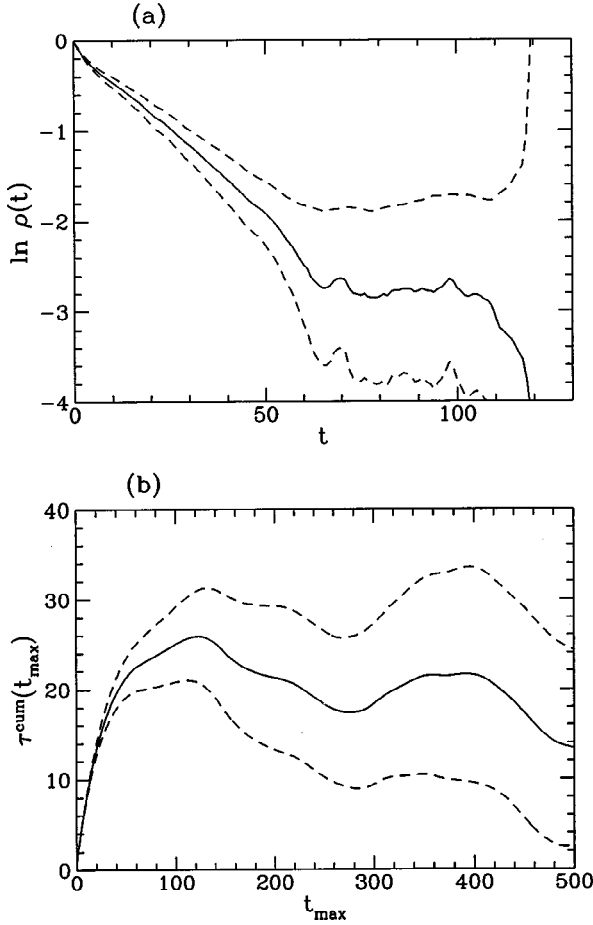


FIG. 1. Autocorrelations for the average plaquette on  $12^3 \times 24$  and  $\kappa^{\text{sea}} = 0.1370$ . (a)  $\ln \rho(t)$  plotted versus  $t$  and (b) the cumulative autocorrelation time plotted against  $t_{\text{max}}$  [see Eq. (19)]. The solid lines follow the computed values for  $\ln \rho(t)$  and  $\tau^{\text{cum}}$ . The dashed lines represent the error bands estimated from a jackknife procedure as described in the text.

The slowest mode of  $\rho_\Omega$  is thus characterized by  $\tau^{\text{exp}}$ , which is relevant for the equilibration of the system. By contrast, the integrated autocorrelation time  $\tau_\Omega^{\text{int}}$  depends on the observable and is required for the estimation of the statistical error in  $\Omega$ , once the system is in equilibrium. It is defined by

$$\tau_\Omega^{\text{int}} = \frac{1}{2} \sum_{t=-\infty}^{\infty} \rho_\Omega(t) = \frac{1}{2} + \sum_{t=1}^{\infty} \rho_\Omega(t), \quad (18)$$

where the latter equality holds since  $\rho_\Omega(-t) = \rho_\Omega(t)$ . This definition implies that statistically independent configurations for the quantity  $\Omega$  are separated by  $2\tau_\Omega^{\text{int}}$ . In practice, one has to truncate the infinite sum in Eq. (18) at some finite value  $t_{\text{max}}$ . The resulting, so-called cumulative autocorrelation time  $\tau_\Omega^{\text{cum}}$ ,

$$\tau_\Omega^{\text{cum}} = \frac{1}{2} + \sum_{t=1}^{t_{\text{max}}} \rho_\Omega(t), \quad (19)$$

is a good approximation to  $\tau_\Omega^{\text{int}}$ , provided that  $t_{\text{max}}$  has been chosen large enough so that any further increase does not

TABLE III. Estimates of autocorrelation times for the average plaquette for  $\beta = 5.2$ , and  $c_{\text{sw}} = 1.76$  on several volumes.

$L^3 \times T$	$\kappa^{\text{sea}}$	No. conf.	$\tau^{\text{cum}}$	$\tau^{\text{exp}}$
$8^3 \times 24$	0.1370	4900	$>20$	$35^{+14}_{-7}$
	0.1380	6700	$44^{+13}_{-10}$	$43^{+3}_{-3}$
	0.1390	6600	$36^{+10}_{-8}$	$53^{+6}_{-6}$
	0.1395	11800	$>57$	$85^{+14}_{-11}$
$12^3 \times 24$	0.1370	6000	$26^{+8}_{-5}$	$29^{+2}_{-2}$
	0.1380	6000	$35^{+16}_{-5}$	$42^{+3}_{-3}$
	0.1390	5600	$52^{+27}_{-25}$	$43^{+5}_{-3}$
	0.1395	5100	$51^{+24}_{-21}$	$51^{+5}_{-4}$
$16^3 \times 24$	0.1390	3800	$38^{+10}_{-9}$	$37^{+3}_{-3}$
	0.1395	4200	$32^{+18}_{-14}$	$27^{+24}_{-9}$
	0.1398	3000	$32^{+23}_{-14}$	$32^{+9}_{-6}$

lead to an increase in  $\tau_\Omega^{\text{cum}}$ . In other words, a plot of  $\tau_\Omega^{\text{cum}}$  versus  $t_{\text{max}}$  should ideally exhibit a plateau for large enough  $t_{\text{max}}$ .

In order to obtain reliable estimates for  $\tau^{\text{exp}}$  and  $\tau_\Omega^{\text{cum}}$ , autocorrelations should ideally be measured using ensembles containing many more configurations than the value of  $\tau_\Omega^{\text{int}}$ . This requirement is not easy to satisfy in simulations whose primary aim is to compute hadronic properties, i.e., for which the calculation of observables requires a non-negligible amount of CPU time. A convenient quantity to determine autocorrelations is the average plaquette, which in our simulations has been measured after every HMC update, and not only on the subset of configurations used to compute quark propagators. Although  $\tau_\Omega^{\text{cum}}$  depends on the quantity  $\Omega$ , the integrated autocorrelation times estimated from the plaquette provide a useful guideline for the computation of hadronic observables.

Examples of our analysis of autocorrelations are shown in Fig. 1. Here the statistical errors plotted for  $\rho(t)$  and  $\tau^{\text{cum}}$  were estimated using a jackknife procedure. In order to take into account the effects of autocorrelations in the error estimate of  $\rho(t)$  and  $\tau^{\text{cum}}$  themselves, the original data for these quantities were grouped in bins of size  $h$ . Jackknife averages were then formed for varying bin sizes, and by increasing  $h$  until the jackknife errors stabilized the error bands in the plots were obtained. Figure 1(a) shows a plot of  $\ln \rho(t)$  versus  $t$ . Here  $\tau^{\text{exp}}$  and its error are extracted from the linear slope at large  $t$  using a fitting routine. Figure 1(b) shows the cumulative autocorrelation time. The central value of  $\tau^{\text{cum}}$  and the error are read off in the region where  $\tau^{\text{cum}}$  shows no significant variation within statistical errors.

Our results for  $\tau^{\text{exp}}$  and  $\tau^{\text{cum}}$  estimated from the average plaquette are shown in Table III. One observes a pronounced dependence of autocorrelation times with the mass of the sea quark. In the range of  $\kappa^{\text{sea}}$  investigated in our study,  $\tau^{\text{exp}}$  and  $\tau^{\text{cum}}$  increase by roughly a factor of 2 as one goes to smaller sea quark masses. Also, a mild volume dependence of  $\tau^{\text{exp}}$  and  $\tau^{\text{cum}}$  is observed, so that autocorrelations appear to be slightly weaker on larger lattices. In view of the large errors, however, this dependence is not really significant.

We have calculated quark propagators on configurations



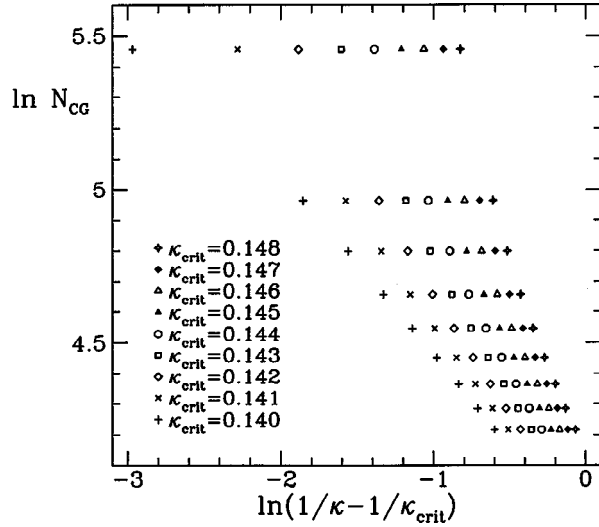


FIG. 2.  $\ln N_{\text{CG}}$  plotted versus  $\ln(1/\kappa - 1/\kappa_{\text{crit}})$  for several trial values of  $\kappa_{\text{crit}}$  for  $\kappa^{\text{sea}} = 0.136$  on  $12^3 \times 24$ .

separated by 60 sweeps on both  $8^3 \times 24$  and  $12^3 \times 24$ , and 40 sweeps on  $16^3 \times 24$ , respectively.

#### E. Scaling of the HMC algorithm and the value of $\kappa_{\text{crit}}$

Here we wish to report briefly on a simple method to obtain an estimate of the critical value of the hopping parameter  $\kappa_{\text{crit}}$  based on the scaling behavior of the HMC algorithm with the quark mass. This method is particularly useful because it can be applied independently of an analysis of spectroscopy data, i.e., without computing any quark propagators at all. We stress, however, that it serves only to obtain a preliminary estimate of  $\kappa_{\text{crit}}$ , whose actual value has to be extracted from the current quark mass or the quark mass behavior of the pseudoscalar meson.

Motivated by the idea that the computer time required for the generation of a dynamical gauge configuration follows a scaling behavior near the critical quark mass, we make the ansatz

$$N_{\text{CG}} \propto \left( \frac{1}{\kappa} - \frac{1}{\kappa_{\text{crit}}} \right)^{\delta}, \quad (20)$$

where  $N_{\text{CG}}$  is the number of conjugate gradient iterations required to invert the fermionic part  $M^{\dagger}M$  to some given accuracy and  $\delta$  is a critical exponent.

If the value of  $\kappa_{\text{crit}}$  is known, we expect that  $\ln N_{\text{CG}}$  plotted against  $\ln(1/\kappa - 1/\kappa_{\text{crit}})$  should be linear with slope  $\delta$ . Conversely, if  $\kappa_{\text{crit}}$  is not known *a priori*, we can use several trial values for  $\kappa_{\text{crit}}$ , taking the value which reproduces the linear behavior of  $\ln N_{\text{CG}}$  as the preliminary estimate of the true  $\kappa_{\text{crit}}$ . Such an analysis is shown in Fig. 2 for  $\kappa^{\text{sea}} = 0.136$  on  $12^3 \times 24$ . Here a straight line is obtained between  $\kappa_{\text{crit}} = 0.140$  and  $0.141$ . This procedure can be optimized by performing a linear fit of  $\ln N_{\text{CG}}$ . For instance, on  $8^3 \times 24$  such a fit yields  $\kappa_{\text{crit}} = 0.14004(4)$ . This is to be compared to the value obtained from the quark mass behavior of the pseudoscalar mass described in Sec. IV, which gives  $\kappa_{\text{crit}}$

$= 0.14047^{+6}_{-7}$ , which is reasonably close to the value obtained from the scaling analysis of the HMC algorithm.

The procedure outlined in this subsection has its merits because many inversions are performed in a typical simulation, and thus a statistically significant value for  $N_{\text{CG}}$  is easily obtained. Strictly speaking, one should only consider the first inversion of the computation of a new trajectory, since this is the only one guaranteed to be performed on a physical configuration (i.e., immediately after the global accept-reject step).

### III. STATIC QUARK POTENTIAL

In this section we describe the computation of the static quark potential using our dynamical configurations. The force between static quarks, calculated from the potential, serves to determine the lattice scale using the hadronic radius  $r_0$  [29]. Furthermore, we study finite-size effects and investigate possible evidence for string breaking.

#### A. General procedure

The method to extract the potential  $V(\mathbf{r})$  from Wilson loops  $W(\mathbf{r}, t)$  of area  $|\mathbf{r}| \times t$  is standard. We have used the algorithm described in [30] to compute “fuzzed” gauge links with a link-staple weighting of 2:1 and between 10 and 20 iterations in the fuzzing algorithm. Using two different fuzzing levels, we have constructed a  $2 \times 2$  variational basis of Wilson loops [31] and subsequently determined the eigenvalues and eigenvectors of the generalized eigenvalue equation [33,34]

$$W_{ij}(\mathbf{r}, t) \phi(\mathbf{r})_j^{(k)} = \lambda^{(k)}(\mathbf{r}; t, t_0) W_{ij}(\mathbf{r}, t_0) \phi(\mathbf{r})_j^{(k)}, \quad i, j, k = 1, 2. \quad (21)$$

The eigenvector  $\phi(\mathbf{r})^{(1)}$ , corresponding to  $\lambda^{(1)}(\mathbf{r}; t, t_0)$  at  $t = 1, t_0 = 0$ , was then used to project onto the approximate ground state [29,32]. This combination of  $(t, t_0)$  turned out to be a compromise between good projection properties and the need to avoid the introduction of additional statistical noise. The resulting correlator was then fitted to both single and double exponentials for time slices up to  $t = 8$ . As a cross-check, we also performed exponential fits to the full  $2 \times 2$  matrix correlator. No significant deviations in the fit parameters as a result of different fitting procedures have been observed.

#### B. Determination of $r_0/a$ on different volumes

The computed values of the potential  $V(\mathbf{r})$  can be used to determine the force  $F(r)$  between a static quark-antiquark pair separated by a distance  $r = |\mathbf{r}|$ . As discussed in [29], the force can be matched at a characteristic scale  $r_0$  to phenomenological potential models describing quarkonia. More precisely,  $r_0$  is defined through the relation

$$F(r_0) r_0^2 = 1.65, \quad (22)$$

TABLE IV. Results for  $r_0/a$  for different lattice sizes and quark masses. The lattice spacing was obtained using  $r_0=0.49$  fm. The first error is the statistical, the second an estimate of the systematic error as described in the text.

$L^3 \times T$	No. conf.	$\kappa^{\text{sea}}$	$r_0/a$	$a$ [fm]
$8^3 \times 24$	119	0.1370	$2.236^{+39}_{-46} +^{59}_{-12}$	$0.2192^{+46}_{-38} +^{11}_{-57}$
	72	0.1380	$2.475^{+74}_{-67} +^{54}_{-23}$	$0.1980^{+53}_{-57} +^{18}_{-43}$
	75	0.1390	$2.891^{+60}_{-58} +^{156}_{-124}$	$0.1695^{+34}_{-35} +^{75}_{-87}$
	125	0.1395	$3.718^{+89}_{-72} +^{75}_{-44}$	$0.1318^{+26}_{-31} +^{15}_{-26}$
	123	0.1370	$2.294^{+20}_{-23} +^{7}_{-2}$	$0.2136^{+22}_{-19} +^{2}_{-7}$
$12^3 \times 24$	110	0.1380	$2.568^{+34}_{-30} +^{34}_{-88}$	$0.1908^{+22}_{-25} +^{67}_{-25}$
	100	0.1390	$3.046^{+58}_{-52} +^{42}_{-7}$	$0.1609^{+28}_{-30} +^{3}_{-22}$
	103	0.1395	$3.435^{+48}_{-47} +^{42}_{-0}$	$0.1426^{+19}_{-20} +^{0}_{-17}$
	100	0.1398	$3.652^{+29}_{-25} +^{7}_{-13}$	$0.1342^{+9}_{-11} +^{6}_{-50}$
	100	0.1390	$3.026^{+32}_{-24} +^{16}_{-0}$	$0.1619^{+13}_{-17} +^{0}_{-8}$
$16^3 \times 24$	90	0.1395	$3.444^{+40}_{-57} +^{26}_{-78}$	$0.1423^{+24}_{-16} +^{30}_{-11}$
	79	0.1398	$3.651^{+31}_{-30} +^{14}_{-12}$	$0.1342^{+11}_{-12} +^{5}_{-5}$

which corresponds to  $r_0 \cong 0.49$  fm. Equation (22) can thus be used together with lattice data for the force to extract  $r_0/a$ , which then yields a value for the lattice scale in physical units. This definition has the advantage that one needs to know the force only at intermediate distances. An extrapolation of the force to infinite separation, which is conventionally performed to extract the string tension, is thus avoided. Hence the procedure is well suited to the case of full QCD, for which the concept of a string tension as the limiting value of the force appears rather dubious, because the string is expected to break at some characteristic distance  $r_b$ .

Our determination of  $r_0/a$  follows closely the procedures described in [29,32]. We have computed the force  $F_d(r_l)$  for orientations  $\mathbf{d}$  of Wilson loops according to

$$F_d(r_l) = |\mathbf{d}|^{-1} [V(\mathbf{r}) - V(\mathbf{r} - \mathbf{d})], \quad (23)$$

$$r_l^2 = -|\mathbf{d}| [G_L(\mathbf{r}) - G_L(\mathbf{r} - \mathbf{d})]^{-1}, \quad (24)$$

where  $G_L(\mathbf{r})$  is the lattice Greens function for one-gluon exchange:

$$G_L(\mathbf{r}) = 4\pi \int_{-\pi}^{\pi} \frac{d^3k}{(2\pi)^3} \frac{\cos(\mathbf{k} \cdot \mathbf{r})}{4 \sum_{j=1}^3 \sin(k_j/2)}. \quad (25)$$

This definition ensures that  $F(r_l)$  is a tree-level improved quantity [29]. In our study we have concentrated on ‘‘on-axis’’ orientations of Wilson loops, i.e., where  $\mathbf{d}=(1,0,0)$ . We have obtained estimates of  $r_0$  in lattice units by a local interpolation of  $F(r_l)r_l^2$  to the point defined in Eq. (22). We emphasize that this procedure does not rely on any model assumptions about the  $r$  dependence of the force.

Systematic errors in  $r_0/a$  were estimated through variations in the interpolation step [e.g., by considering a third data point for  $F(r_l)r_l^2$  besides those which straddle 1.65] and also by using alternative fitting procedures in the extraction of the potential (e.g., single or double exponential fits, dif-

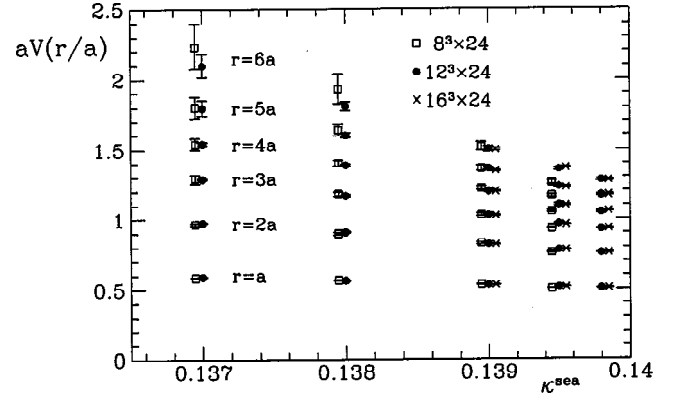


FIG. 3. Static quark potential for the first six on-axis separations  $r/a=1,\dots,6$  plotted against  $\kappa^{\text{sea}}$  for different lattice sizes.

ferent fitting intervals). We note that the systematic error in  $r_0/a$ , in particular for smaller values of the sea quark mass, is dominated by the uncertainty incurred by considering different points in the interpolation step. A summary of our results on all lattices and for all values of  $\kappa^{\text{sea}}$  is shown in Table IV. The configurations on which the potential has been determined were separated by 40 HMC trajectories for all lattice sizes and quark masses.

The comparison of results obtained on the  $8^3 \times 24$  and  $12^3 \times 24$  lattices shows that there are pronounced finite-size effects at  $\kappa^{\text{sea}}=0.1395$ , whereas for larger quark masses these effects are small. The presence or absence of finite-size effects is easily recognized in the values of the potential  $V(\mathbf{r})$  itself, as shown in Fig. 3. On the other hand, there is remarkable agreement in the data obtained on  $16^3 \times 24$  and  $12^3 \times 24$ , even at the lightest quark mass considered. This is illustrated in Fig. 4, where the results of  $r_0/a$  on all lattices are plotted against  $1/\kappa^{\text{sea}}$ . Our findings can be translated into a bound on  $L/r_0$ , above which finite-size effects in the static quark potential are largely absent at this level of precision. From our results we infer that the bound is

$$L/r_0 \gtrsim 3.2, \quad (26)$$

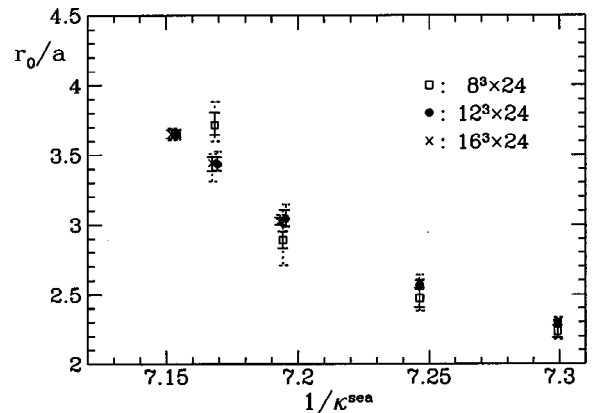


FIG. 4. Hadronic scale  $r_0/a$  plotted against  $1/\kappa^{\text{sea}}$  for different lattice sizes. The chiral limit is approximately at the left margin of the figure. Solid error bars represent the statistical errors, whereas the dotted error bars denote the linearly added systematic error.

which, for instance, is still satisfied for  $\kappa^{\text{sea}} \leq 0.1380$  on  $8^3 \times 24$ . This bound, however, should not be generalized *prima facie* to other quantities, in particular the spectrum of hadronic states discussed in Sec. IV, for which finite-volume effects could well be different. We will return to this point in Sec. IV C.

Figure 4 shows that the data for  $r_0/a$  obtained at the three lightest quark masses on  $L/a = 12$  and 16 show a linear behavior. We have therefore attempted a linear extrapolation of  $r_0/a$  to the chiral limit using the data at  $\kappa^{\text{sea}} = 0.1390$ , 0.1395, and 0.1398 only, despite the lack of a theoretical motivation as to why such an ansatz for the quark mass dependence of  $r_0/a$  should be valid. Taking into account only statistical errors in  $r_0/a$ , the extrapolations for  $L/a = 12, 16$  yield

$$L/a = 12: \quad r_0/a = 4.10 \pm 0.06, \quad a = 0.122 \pm 0.002 \text{ fm}, \quad (27)$$

$$L/a = 16: \quad r_0/a = 4.15 \pm 0.06, \quad a = 0.121 \pm 0.002 \text{ fm}. \quad (28)$$

Thus the overall box sizes in the chiral limit amount to 1.46(2) fm for  $L/a = 12$  and 1.93(3) fm for  $L/a = 16$ . A comparison with data for  $r_0/a$  obtained in the quenched approximation shows that our estimates in the chiral limit for  $n_f = 2$  massless quarks at  $\beta = 5.2$ ,  $c_{\text{sw}} = 1.76$  roughly correspond to values around  $\beta = 5.85 - 5.9$  in quenched QCD [35,36].

### C. Is there evidence for dynamical quark effects?

We now examine our data for the static quark potential for possible evidence for the effects of dynamical quarks. In Fig. 5(a) we show the potential in units of  $r_0$ , normalized to  $V(r_0)$ , for five values of  $\kappa^{\text{sea}}$  used on  $12^3 \times 24$ . We compare our results to the expression

$$[V(r) - V(r_0)]r_0 = (1.65 - e) \left( \frac{r}{r_0} - 1 \right) - e \left( \frac{r_0}{r} - 1 \right), \quad (29)$$

which follows from the standard linear-plus-Coulomb ansatz for  $V(r)$ , viz.,

$$V(r) = V_0 + \sigma r - \frac{e}{r}, \quad (30)$$

and the condition (22). Here  $\sigma$  denotes the string tension and we have set  $e = \pi/12$  [37], so that the solid line in the figure has not been obtained through a fit. The data at different  $\kappa^{\text{sea}}$  have been offset by  $V(r_0)$ , whose value was obtained by a local interpolation of the potential.

In the presence of dynamical quarks, one expects a deviation of the data at large separations from the linear behavior described by the curve in Eq. (29), so that the potential in full QCD flattens out due to string breaking. For separations larger than the breaking scale  $r_b$ , one expects that the potential is equal to the mass of two ‘‘mesons,’’ consisting of a static quark and a light antiquark, i.e., the energy of a state

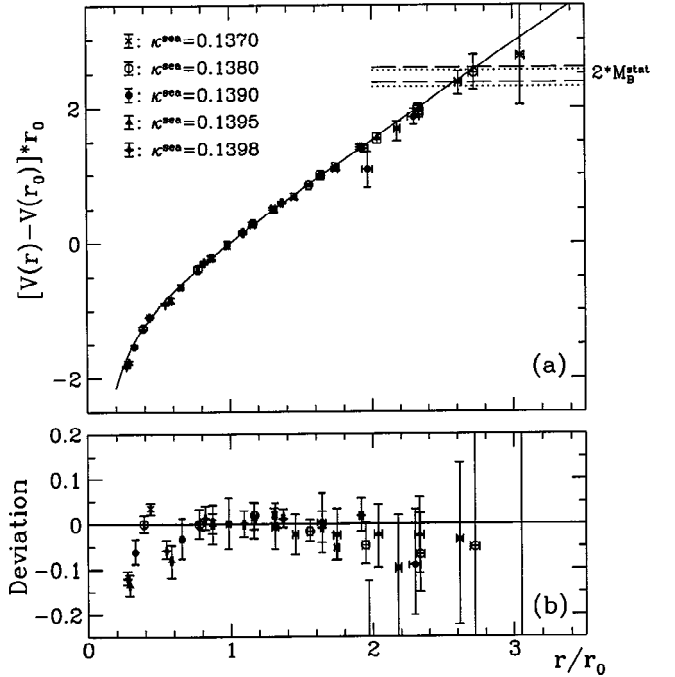


FIG. 5. (a) Scaled and normalized potential as a function of  $r/r_0$  as obtained on  $12^3 \times 24$ . The solid curve is the prediction from Eq. (29). (b) Deviation between the data points and Eq. (29).

corresponding to a broken string. The masses of such static-light mesons have been calculated on  $12^3 \times 24$  for  $\kappa^{\text{sea}} = 0.1390$  and 0.1395 using the technique described in [38]. The error bands of this determination are shown as the dotted ( $\kappa^{\text{sea}} = 0.1395$ ) and dashed ( $\kappa^{\text{sea}} = 0.1390$ ) lines in Fig. 5 (a).

Our data for the potential for distances  $r > 1$  fm are neither in disagreement with the curve in Eq. (29) nor with the expected asymptotic value of  $2M_B^{\text{static}}$ . In order to check whether more statistics could help in revealing the flattening of the potential at large distances, we have computed the potential on 194 stored HMC trajectories for  $\kappa^{\text{sea}} = 0.1395$  on our larger lattice size of  $16^3 \times 24$ , but no qualitative change compared to the data in Fig. 5(a) could be detected. Thus there is at present no conclusive evidence for string breaking at length scales up to  $r \approx 1.5$  fm. There are a number of arguments why this is so. First, we wish to stress that the data points which probe the largest separations in Fig. 5 have typically been obtained using smaller values of  $\kappa^{\text{sea}}$ , for which the sea quarks may still be too heavy in order to produce a significantly different qualitative behavior of  $V(r)$ .

It has also been argued [2] that the Wilson loop used to extract  $V(r)$  does not project well onto states of broken strings. This has, in fact, been confirmed in simulations using bosonic matter fields [39,40]. In QCD, further investigations of this issue are required, in particular for smaller sea quark masses. Without a clear demonstration of string breaking, we can only give a rough estimate for the breaking scale  $r_b$  from the intersection of the data of the potential with the value  $2M_B^{\text{static}}$ . From Fig. 5(a), we read off  $r_b \approx 2.6r_0$ .

At small distances, where the potential is dominated by the Coulombic part, we find that the expression in Eq. (29) still describes the data surprisingly well, although the points

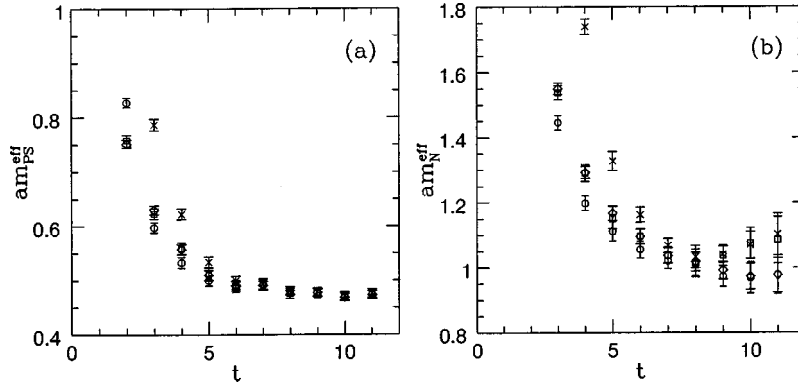


FIG. 6. Effective mass plots on a  $12^3 \times 24$  volume for  $\kappa^{\text{sea}} = \kappa^{\text{val}} = 0.1398$ . In (a) the pseudoscalar and in (b) the nucleon are shown for different fuzzing combinations, i.e., FF ( $\circ$ ), FL ( $\diamond$ ), LF ( $\square$ ), and LL ( $\times$ ).

obtained for the three lightest quark masses have a tendency to lie somewhat below the curve at the smallest separations. This is highlighted in Fig. 5(b) where the deviation between the data points and Eq. (29) is plotted. It implies that the data at small distances and quark masses seem to favor a larger value for  $e$  compared to  $e = \pi/12$  in the pure gauge theory, as has been observed also in [5]. This qualitative observation is consistent with the expected influence of dynamical quarks on the short-distance regime of the potential through the  $n_f$  dependence in the running of the strong coupling constant.

However, if one wants to quantify the change in  $e$ , one should take into account the lattice Greens function  $G_L(\mathbf{r})$  for one-gluon exchange in order to account for lattice artifacts at small distances. If  $r_0/r$  in the last term of Eq. (29) is replaced by  $r_0 G_L(\mathbf{r})$ , the observed deviations for  $r/r_0 \leq 0.8$  are slightly smaller, but still significant. At every value of  $\kappa^{\text{sea}}$ , we have translated the difference between the data points and the theoretical prediction [using Eq. (29) with  $r/r_0$  replaced by  $r_0 G_L(\mathbf{r})$ ] into an estimate for the favored value of  $e$ . At  $\kappa^{\text{sea}} = 0.1398$  we estimate that the enhancement of  $e$  over its value in the bosonic string model amounts to about 7%.

This is only a crude analysis of sea quark effects in the short-distance part of the potential. In principle, these effects on the running coupling could be probed by computing the coupling constant from the force according to

$$\alpha(r) \equiv \frac{3}{4} F(r) r^2 \quad (31)$$

and comparing its scale dependence to the two-loop perturbative  $\beta$  function for  $n_f = 2$ . In view of the many caveats concerning our present data, such as the fairly large length scales, the relatively heavy sea quarks, and the lack of a continuum extrapolation, we have not seriously attempted such an analysis at this stage.

To summarize, as far as the issue of string breaking is concerned, we find no hard evidence for the effects of dynamical quarks for distances up to 1.5 fm in the static quark potential. However, there are indications of a qualitatively different behavior in the Coulombic range at small distances, which is hard to quantify and corroborate with the present data.

#### IV. HADRON SPECTROSCOPY

In this section we describe the computation of the light hadron spectrum. The simulation parameters used have been discussed in Sec. II C.

##### A. Analysis and fitting procedure

The amplitudes and masses of hadrons are obtained in a standard way by correlated least- $\chi^2$  fits of the correlation functions. The fitting function used was different for mesonic and baryonic channels. In the mesonic case, we have taken into account the backward propagating particle on a periodic lattice by fitting to the function

$$C_M(t) = A_0(e^{-m_0 t} + e^{m_0(T-t)}) + A_1(e^{-m_1 t} + e^{m_1(T-t)}), \quad (32)$$

where  $A_i$ ,  $m_i$ ,  $i=0,1$ , are the amplitudes and masses of the ground and first excited states. In the baryonic case, we have used

$$C_B(t) = A_0 e^{-m_0 t} + A_1 e^{-m_1 t}. \quad (33)$$

We have computed hadronic two-point correlation functions with different combinations of “fuzzing” [26] both at source and at sink: we denote as FF the correlator fuzzed at source and sink, FL fuzzed only at source, etc. We have found that the FF correlator allows the fastest isolation of the fundamental state, even in the case of the lightest  $\kappa$ 's in which the effect of fuzzing is most important. To illustrate this point, we show in Fig. 6 the effective mass plots of the pseudoscalar and the nucleon for  $\kappa^{\text{sea}} = \kappa^{\text{val}} = 0.1398$  on a  $12^3 \times 24$  volume. We conclude that the effect of fuzzing is quite significant compared with the LL case, as also found in the quenched approximation [42]. We have fitted simultaneously the LL and FF correlators to a double exponential functional form, using the difference between the correlators to control the first excited state.

The quantity  $\chi^2/N_{\text{DF}}$  used to monitor the quality of a correlated fit is known to suffer from a systematic bias, which depends on the degree of freedom and the statistics [41]. We have implemented the technique of eigenvalue smoothing [41] in the computation of the correlation matrix to take this bias into account. We have performed a “sliding



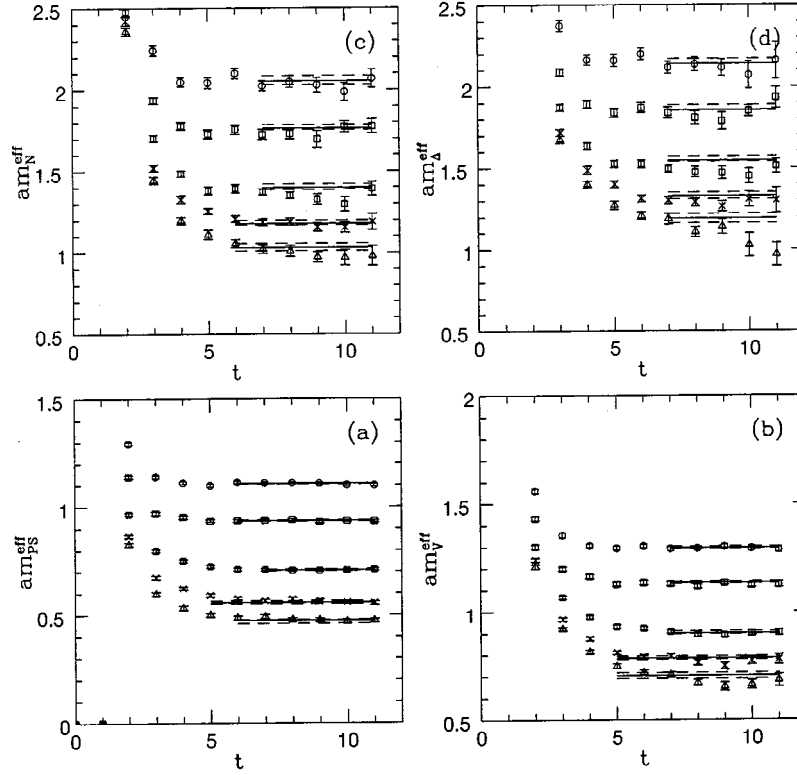


FIG. 7. Effective mass plots for the pseudoscalar (a), vector (b), nucleon (c), and  $\Delta$  (d), on a  $12^3 \times 24$  volume for all values of  $\kappa^{\text{sea}}$ . The effective mass has been calculated from the FF correlator with  $\kappa^{\text{sea}} = \kappa^{\text{val}}$ . Solid lines denote the fitted value of the mass, obtained from a simultaneous fit to the FF and LL correlators. The dashed lines denote the error band, and the length of the lines indicates the fit interval.

window'' analysis, fixing the maximum value of the fit interval, i.e.,  $t_{\text{max}} = 11$ , and varying  $t_{\text{min}}$  to monitor the optimal interval. The stability criterion we have used is that the hadron mass should not change appreciably as  $t_{\text{min}}$  is changed by one unit. The value of  $t_{\text{min}}$  has been determined for each different combination of  $\kappa^{\text{sea}}$  and  $\kappa^{\text{val}}$ .

### B. Dynamical spectrum

In a numerical simulation with dynamical fermions, the parameters  $\kappa^{\text{sea}}$  and  $\kappa^{\text{val}}$  are distinct and each set of configurations generated for different  $\kappa^{\text{sea}}$  is independent. We have performed the analysis of the hadron spectrum for each fixed value of  $\kappa^{\text{sea}}$ . At an intermediate level, these simulations can be thought of as "pseudoquenched," which come closer to the description of the real world as the sea quark mass approaches its physical value. There is another reason why we found it useful to simulate different values of  $\kappa^{\text{val}}$  for each  $\kappa^{\text{sea}}$ ; cf. Table II. We interpret the heavier  $\kappa$ 's as describing the valence quarks, in particular the strange, in the sea of light quarks, i.e., the up and down.

In Fig. 7 we show the effective mass plots on a  $12^3 \times 24$  volume for the pseudoscalar, vector, nucleon, and  $\Delta$ , obtained for  $\kappa^{\text{sea}} = \kappa^{\text{val}}$ . The pseudoscalar shows a clear plateau at all values of the hopping parameter, whereas for the vector the plateau becomes more unstable at the lightest quark masses. In the baryonic channels, on the other hand, the plateaux are, as expected, more fluctuating and we require a longer lattice in the time direction.

In the tables given in the Appendix, we summarize the results for the hadron masses obtained on the different volumes. We give the masses both in lattice units and in units of  $r_0$ , the latter being more significant in the comparison between different volumes, as it compensates for the sea quark dependence of the lattice spacing.

In Table V we list the values of the mass ratio of pseudoscalar and vector mesons,  $m_{\text{PS}}/m_V$ , obtained for  $\kappa^{\text{val}} = \kappa^{\text{sea}}$ , which is a measure of how heavy our dynamical quark masses are relative to the real up and down quarks. Given that our lightest sea quark produces  $m_{\text{PS}}/m_V \approx 0.67$ , we conclude that the sea quarks used in our simulation are still relatively heavy.

A useful quantity is the critical value of the hopping parameter  $\kappa_{\text{crit}}$ . Here we have used our data for pseudoscalar mesons, computed for  $\kappa^{\text{val}} = \kappa^{\text{sea}}$  and determined  $\kappa_{\text{crit}}$  from a fit

TABLE V. Ratio  $m_{\text{PS}}/m_V$  for  $\kappa^{\text{sea}} = \kappa^{\text{val}}$  on the two largest lattice sizes.

$\kappa^{\text{sea}}$	$L=12$ $m_{\text{PS}}/m_V$	$L=16$ $m_{\text{PS}}/m_V$
0.1370	$0.855^{+2}_{-3}$	
0.1380	$0.825^{+4}_{-5}$	
0.1390	$0.785^{+4}_{-7}$	$0.785^{+6}_{-7}$
0.1395	$0.710^{+10}_{-10}$	$0.719^{+7}_{-10}$
0.1398	$0.674^{+9}_{-23}$	$0.670^{+10}_{-13}$

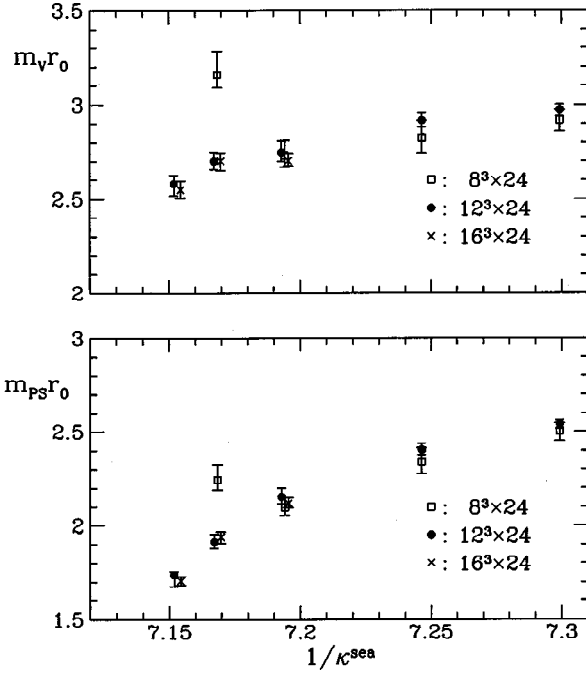


FIG. 8. Vector and pseudoscalar masses, in units of  $r_0$ , as a function of  $1/\kappa^{\text{sea}} = 1/\kappa^{\text{val}}$  for different volumes.

$$(am_{\text{PS}})^2 = aB(a\tilde{m}_q), \quad (34)$$

where

$$\tilde{m}_q = m_q(1 + b_m am_q), \quad am_q = \frac{1}{2} \left( \frac{1}{\kappa^{\text{sea}}} - \frac{1}{\kappa^{\text{crit}}} \right). \quad (35)$$

Since  $b_m$  has not been determined nonperturbatively, we have used its perturbative expression at one loop [43]:

$$b_m = -\frac{1}{2} - 0.0962g_0^2. \quad (36)$$

We considered this choice sufficient for our purposes, given that the value for  $c_{\text{sw}}$  used in this study does not completely remove the leading cutoff effects. For every lattice size we fitted the three most chiral points to Eq. (34), and the results for  $\kappa_{\text{crit}}$  are

$$L/a = 8: \quad \kappa_{\text{crit}} = 0.14047_{-7}^{+6}, \quad (37)$$

$$L/a = 12: \quad \kappa_{\text{crit}} = 0.14040_{-6}^{+2}, \quad (38)$$

$$L/a = 16: \quad \kappa_{\text{crit}} = 0.14043_{-3}^{+2}. \quad (39)$$

As an aside, we remark that the results for  $\kappa_{\text{crit}}$  obtained using  $b_m = 0$  in Eq. (35) are entirely compatible with these values within errors.

Traditionally, the way to make contact with the physical values of the light hadron spectrum in quenched simulations has been to extrapolate the masses, obtained at several values of  $\kappa$ , to the chiral limit. For example, the lattice spacing has usually been determined by extrapolation of the vector mass and the physical value of  $m_\rho$ . This approach is safe as long

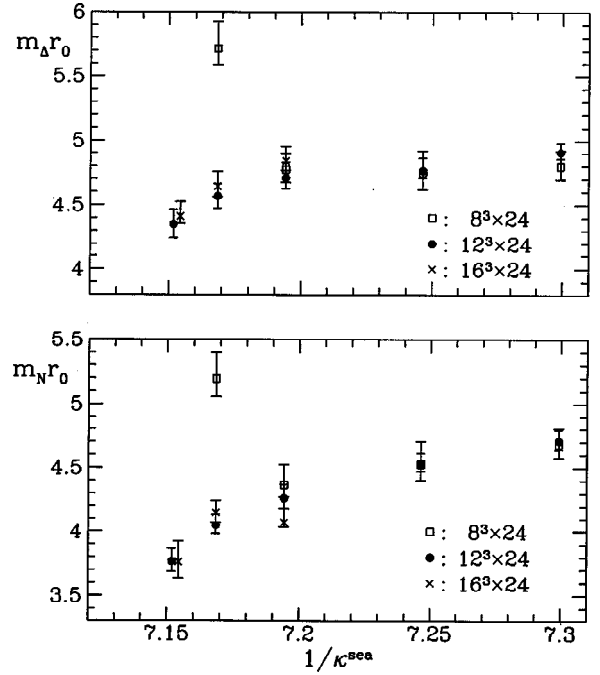


FIG. 9.  $\Delta$  and nucleon masses, in units of  $r_0$ , as a function of  $1/\kappa^{\text{sea}} = 1/\kappa^{\text{val}}$  for different volumes.

as the particles have zero decay width, as in the quenched approximation, but is no longer feasible in the dynamical case in which the  $\rho$  is not stable. Hence it is desirable to avoid extrapolations to the chiral limit, whenever possible. With this viewpoint, it has been proposed in [44,45] to extract physical values from the region of the strange quark.

### C. Finite-size effects in the spectrum

As already mentioned in the Introduction, one of the aims of this study is to acquire experience of the systematics in dynamical simulations with improved fermions, even if the  $O(a)$  effects are not entirely removed. One important feature to address is the presence of finite-size effects in the spectrum, which determines the volume at which we can reliably carry out the calculation. Finite-size effects in dynamical simulations of hadronic spectrum with Wilson-like fermions have not been studied in great detail. The only results are those of the SESAM and T $\chi$ L Collaborations with an unimproved fermionic action, exploring volumes  $16^3 \times 32$  and  $24^3 \times 40$  [11]. It is thus important to study and quantify these effects using an  $O(a)$  improved action.

In Figs. 8 and 9 we show the volume dependence of the meson and baryon masses, in units of  $r_0$ , as a function of  $1/\kappa^{\text{sea}}$ , for  $\kappa^{\text{sea}} = \kappa^{\text{val}}$ . It confirms the behavior already found in the study of the static quark potential. That is, we find pronounced finite-size effects between  $8^3 \times 24$  and  $12^3 \times 24$ , which can grow up to 15–17% in the mesonic sector and up to 25–28% in the baryonic sector, as we move towards the most chiral point. On the other hand, between  $12^3 \times 24$  and  $16^3 \times 24$  we find no significant discrepancy within statistical accuracy at all common values of the quark mass. From the similarity of the finite-size behavior of meson masses and the

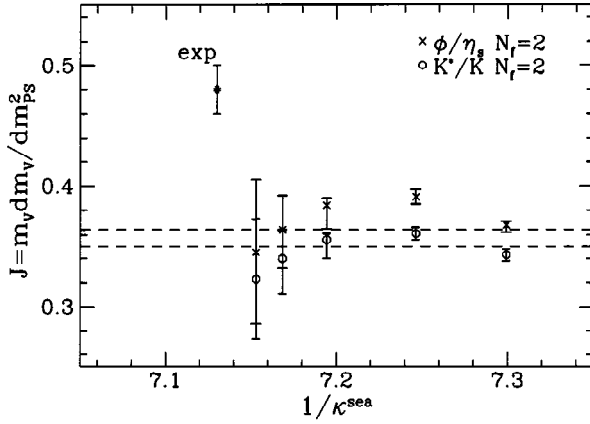


FIG. 10. Values of the parameter  $J$ , determined from fixing the  $K^*/K$  and  $\phi/\eta_s$ , plotted against  $1/\kappa^{\text{sea}}$  for  $V=12^3 \times 24$ . The quenched result, taken from [46], is represented by the dashed lines.

static quark potential discussed in Sec. III, we conclude that the bound, Eq. (26), is also valid for simple hadronic quantities.

#### D. Sea quark effects in the spectrum

The parameter  $J$  has been introduced in [44] as a way to quantify the discrepancy between the quenched spectrum and experiment. It is defined as

$$J = m_{K^*} \frac{dm_V}{dm_{\text{PS}}^2} \quad (40)$$

and has the attractive feature that it is dimensionless, does not involve extrapolations to the chiral limit, and is independent of the quark mass value chosen to evaluate it, provided that  $m_V$  depends linearly on  $m_{\text{PS}}^2$ . The only physical prediction sacrificed to calculate  $J$  is the ratio  $m_{K^*}/m_K = 1.81$ . In the  $(m_{\text{PS}}^2, m_V)$  plane, this corresponds to a parabola, the intercept of which with the linear interpolation of the stimulated data yields the point  $(m_{\text{PS}}^2, m_{K^*})$  of strange mesons. An alternative way to determine  $J$  is to use mesons with full strange valence quark content, by assuming that the  $\eta_s$  is purely  $s\bar{s}$  and that  $m_\phi/m_{\eta_s} = 1.49$ .

We emphasize that a realistic evaluation of  $J$  in the dynamical case is not straightforward. As pointed out in [44], it would not be appropriate to compare meson masses obtained using different dynamical quark masses as the lattice spacing  $a$  depends on the sea quark mass. Our approach has been to fix the sea quark mass and for each sea quark consider different valence quark masses. Ideally, since we are looking to interpret the valence quarks as having strange flavor in the sea of light quarks, we would need to consider values of  $\kappa^{\text{val}} < \kappa^{\text{sea}}$ . With our present data set, this is only possible at the most chiral sea quark masses. However, since even our lightest sea quark mass is in the region of that of the strange quark, we do not expect the values of  $J$  to be significantly closer to the experimental value of  $J = 0.48(2)$ , compared to the quenched approximation.

In Fig. 10 we show the values of  $J$  and compare them

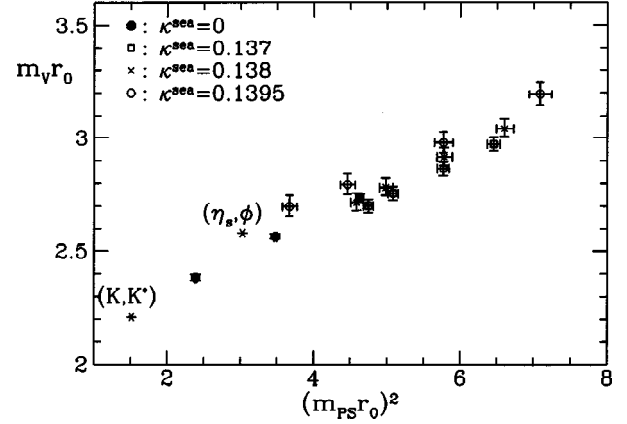


FIG. 11. Vector mass plotted against the pseudoscalar mass for  $V=12^3 \times 24$  for several sets of different sea quark masses. Asterisks denote the experimental points. The quenched results (labeled  $\kappa^{\text{sea}} = 0$ ) are taken from [46].

with the quenched result at  $\beta=5.7$  and  $V=12^3 \times 24$  [46]. The values of  $J$ , obtained by either fixing  $m_{K^*}/m_K$  or  $m_\phi/m_{\eta_s}$ , show no appreciable trend towards the experimental point as the sea quark mass decreases. However, a reliable and precise evaluation of  $J$  is becoming more difficult for decreasing sea quark mass; the statistical error in the slope  $dm_V/dm_{\text{PS}}^2$  gets rapidly larger, and furthermore the value of  $J$  is increasingly dependent on the set of valence quark masses used in its determination. Where necessary we have included this dependence as a systematic error, which has been added in quadrature to the errors shown in Fig. 10. We conclude that although a clear trend towards the phenomenological result for  $J$  is not observed, the deviation for the lightest sea quarks is less significant.

Another way to look for dynamical quark effects in the light hadron spectrum, which does not involve any fitting, is to concentrate directly on the plot of the vector mass versus the pseudoscalar mass squared. This is shown in Fig. 11. As the sea quark mass is decreased relative to the valence quark mass, one observes a significant, albeit small, trend of the

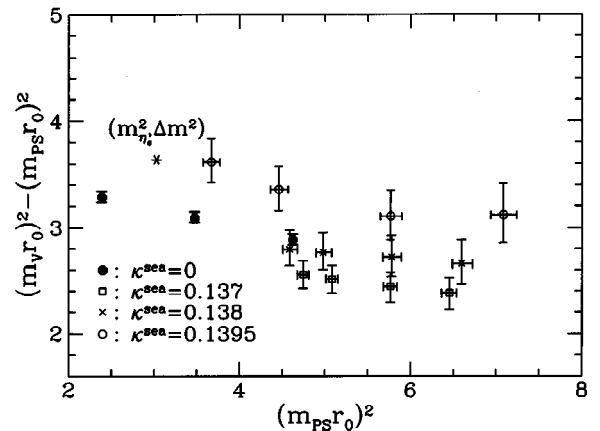


FIG. 12. Hyperfine splitting  $(m_V r_0)^2 - (m_{\text{PS}} r_0)^2$  plotted against  $(m_{\text{PS}} r_0)^2$  for  $V=12^3 \times 24$ . The quenched results ( $\kappa^{\text{sea}} = 0$ ) are taken from [46].

TABLE VI. Pseudoscalar masses on  $8^3 \times 24$ , in lattice units and in units of  $r_0$ .

$L^3 \times T$	$\kappa^{\text{sea}}$	$\kappa^{\text{val}}$	$m_{\text{PS}}a$	$m_{\text{PS}}r_0$	Fit	$\chi^2/N_{\text{DF}}$
$8^3 \times 24$	0.1370	0.1370	$1.119^{+8}_{-4}$	$2.502^{+47}_{-52}$	[6,11]	12.70/6
		0.1380	$1.059^{+8}_{-4}$	$2.368^{+45}_{-50}$	[6,11]	12.77/6
		0.1390	$0.997^{+9}_{-5}$	$2.229^{+44}_{-47}$	[6,11]	13.20/6
		0.1395	$0.965^{+9}_{-5}$	$2.158^{+43}_{-45}$	[6,11]	13.57/6
$8^3 \times 24$	0.1380	0.1370	$1.011^{+10}_{-2}$	$2.502^{+79}_{-68}$	[5,11]	14.94/8
		0.1380	$0.945^{+11}_{-2}$	$2.339^{+75}_{-64}$	[5,11]	13.28/8
		0.1390	$0.874^{+12}_{-6}$	$2.164^{+72}_{-61}$	[5,11]	7.26/8
		0.1395	$0.840^{+14}_{-6}$	$2.078^{+71}_{-58}$	[5,11]	7.50/8
$8^3 \times 24$	0.1390	0.1370	$0.870^{+9}_{-5}$	$2.514^{+58}_{-53}$	[6,11]	8.14/6
		0.1380	$0.799^{+10}_{-5}$	$2.309^{+57}_{-49}$	[6,11]	8.18/6
		0.1390	$0.726^{+11}_{-6}$	$2.099^{+53}_{-45}$	[5,11]	10.24/8
		0.1395	$0.686^{+12}_{-5}$	$1.982^{+53}_{-43}$	[5,11]	10.86/8
$8^3 \times 24$	0.1395	0.1370	$0.786^{+9}_{-14}$	$2.924^{+78}_{-78}$	[6,11]	9.70/6
		0.1380	$0.710^{+9}_{-12}$	$2.640^{+72}_{-68}$	[6,11]	10.75/6
		0.1390	$0.642^{+15}_{-10}$	$2.387^{+80}_{-60}$	[5,11]	15.07/8
		0.1395	$0.603^{+17}_{-7}$	$2.242^{+82}_{-51}$	[4,11]	17.30/10

meson masses towards the point  $(m_{\eta_s}^2, m_{\phi})$ , i.e., the pair of mesons, whose valence quark content resembles most closely that used in our simulation. Concentrating on the lighter sea quark mass, e.g.,  $\kappa^{\text{sea}}=0.1395$ , we can assert a significant shift compared to the quenched result, at  $\beta=5.7$  and  $V=12^3 \times 24$  [46]. Figure 11 also shows that the slopes of the data sets at fixed  $\kappa^{\text{sea}}$  show little variation. This explains why we do not observe much improvement in the value of  $J$ ,

TABLE VII. Pseudoscalar masses on  $12^3 \times 24$ , in lattice units and in units of  $r_0$ .

$L^3 \times T$	$\kappa^{\text{sea}}$	$\kappa^{\text{val}}$	$m_{\text{PS}}a$	$m_{\text{PS}}r_0$	Fit	$\chi^2/N_{\text{DF}}$
$12^3 \times 24$	0.1370	0.1370	$1.108^{+3}_{-2}$	$2.541^{+23}_{-26}$	[6,11]	9.93/6
		0.1380	$1.047^{+3}_{-2}$	$2.402^{+22}_{-25}$	[5,11]	11.18/8
		0.1390	$0.983^{+4}_{-2}$	$2.255^{+21}_{-23}$	[5,11]	11.65/8
		0.1395	$0.950^{+4}_{-3}$	$2.179^{+21}_{-23}$	[5,11]	11.83/8
$12^3 \times 24$	0.1380	0.1370	$1.000^{+3}_{-2}$	$2.569^{+35}_{-30}$	[6,11]	10.41/6
		0.1380	$0.936^{+3}_{-2}$	$2.404^{+33}_{-29}$	[6,11]	10.79/6
		0.1390	$0.869^{+4}_{-2}$	$2.232^{+31}_{-27}$	[6,11]	11.37/6
		0.1395	$0.834^{+4}_{-2}$	$2.142^{+30}_{-26}$	[6,11]	11.56/6
$12^3 \times 24$	0.1390	0.1370	$0.858^{+4}_{-3}$	$2.613^{+51}_{-45}$	[7,11]	5.93/4
		0.1380	$0.785^{+4}_{-3}$	$2.391^{+48}_{-42}$	[7,11]	4.16/4
		0.1390	$0.707^{+5}_{-3}$	$2.155^{+44}_{-38}$	[7,11]	2.69/4
		0.1395	$0.669^{+5}_{-3}$	$2.037^{+42}_{-36}$	[6,11]	16.86/6
$12^3 \times 24$	0.1395	0.1370	$0.775^{+6}_{-4}$	$2.662^{+42}_{-39}$	[7,11]	21.46/4
		0.1380	$0.699^{+5}_{-4}$	$2.402^{+38}_{-36}$	[6,11]	26.14/6
		0.1390	$0.615^{+6}_{-4}$	$2.112^{+36}_{-32}$	[6,11]	19.70/6
		0.1395	$0.558^{+8}_{-7}$	$1.916^{+38}_{-35}$	[5,11]	8.96/8
$12^3 \times 24$	0.1398	0.1380	$0.639^{+5}_{-4}$	$2.332^{+27}_{-21}$	[7,11]	3.63/4
		0.1390	$0.551^{+4}_{-9}$	$2.011^{+23}_{-37}$	[7,11]	2.09/4
		0.1395	$0.492^{+3}_{-9}$	$1.797^{+18}_{-36}$	[6,11]	3.41/6
		0.1398	$0.476^{+3}_{-16}$	$1.738^{+17}_{-61}$	[6,11]	8.14/6

TABLE VIII. Pseudoscalar masses on  $16^3 \times 24$ , in lattice units and in units of  $r_0$ .

$L^3 \times T$	$\kappa^{\text{sea}}$	$\kappa^{\text{val}}$	$m_{\text{PS}}a$	$m_{\text{PS}}r_0$	Fit	$\chi^2/N_{\text{DF}}$
$16^3 \times 24$	0.1390	0.1390	$0.701^{+6}_{-5}$	$2.120^{+30}_{-22}$	[6,11]	10.62/6
		0.1395	$0.660^{+6}_{-4}$	$1.998^{+28}_{-21}$	[6,11]	9.31/6
		0.1398	$0.635^{+6}_{-5}$	$1.922^{+27}_{-22}$	[6,11]	8.34/6
$16^3 \times 24$	0.1395	0.1390	$0.610^{+4}_{-2}$	$2.101^{+28}_{-36}$	[6,11]	7.04/6
		0.1395	$0.564^{+3}_{-4}$	$1.942^{+25}_{-36}$	[6,11]	3.05/6
		0.1398	$0.537^{+4}_{-3}$	$1.848^{+32}_{-32}$	[7,11]	2.99/4
$16^3 \times 24$	0.1398	0.1390	$0.551^{+5}_{-5}$	$2.011^{+26}_{-26}$	[7,11]	10.66/4
		0.1395	$0.502^{+5}_{-6}$	$1.834^{+24}_{-28}$	[7,11]	8.48/4
		0.1398	$0.468^{+5}_{-5}$	$1.707^{+23}_{-24}$	[7,11]	6.02/4

in spite of the closer proximity of the data at smaller  $\kappa^{\text{sea}}$  relative to the experimental point.

At this stage it is hard to quantify the observed shift and to disentangle the genuine sea quark effect from residual lattice artifacts, which could be fairly large in these simulations. A suitable approach would be to monitor dynamical quark effects at fixed lattice spacing. Starting from the quenched approximation and going to ever lighter sea quark masses, one would have to perform a sequence of simulations, which are matched such that they all reproduce the same value of a suitable lattice scale, e.g.,  $r_0$  [47]. Results will be published in a future publication, using the fully  $O(a)$  improved action for dynamical and quenched simulations [18].

Another quantity, which can be used to highlight the effects of dynamical quarks, is the vector-pseudoscalar mass splitting. It is well known that lattice simulations fail to reproduce the experimental fact that this hyperfine splitting is constant over a large range of quark masses,  $m_V^2 - m_{\text{PS}}^2 \approx 0.55 \text{ GeV}^2$ . The discrepancy between the experimental and

TABLE IX. Vector masses on  $8^3 \times 24$ , in lattice units and in units of  $r_0$ .

$L^3 \times T$	$\kappa^{\text{sea}}$	$\kappa^{\text{val}}$	$m_Va$	$m_Vr_0$	Fit	$\chi^2/N_{\text{DF}}$
$8^3 \times 24$	0.1370	0.1370	$1.305^{+11}_{-6}$	$2.917^{+57}_{-61}$	[7,11]	5.82/4
		0.1380	$1.257^{+12}_{-6}$	$2.810^{+56}_{-59}$	[7,11]	5.09/4
		0.1390	$1.209^{+14}_{-7}$	$2.703^{+56}_{-58}$	[7,11]	5.27/4
$8^3 \times 24$	0.1395	0.1370	$1.185^{+14}_{-8}$	$2.650^{+56}_{-57}$	[7,11]	5.78/4
		0.1380	$1.190^{+14}_{-7}$	$2.946^{+95}_{-82}$	[6,11]	7.30/6
		0.1390	$1.140^{+15}_{-8}$	$2.822^{+92}_{-79}$	[6,11]	7.68/6
$8^3 \times 24$	0.1390	0.1370	$1.090^{+16}_{-9}$	$2.697^{+90}_{-76}$	[6,11]	9.02/6
		0.1395	$1.064^{+17}_{-10}$	$2.634^{+89}_{-76}$	[6,11]	10.05/6
		0.1398	$1.045^{+13}_{-7}$	$3.022^{+72}_{-64}$	[7,11]	5.21/4
$8^3 \times 24$	0.1390	0.1370	$0.998^{+16}_{-9}$	$2.885^{+76}_{-64}$	[6,11]	6.49/6
		0.1380	$0.944^{+19}_{-10}$	$2.730^{+79}_{-61}$	[6,11]	4.66/6
		0.1395	$0.918^{+20}_{-10}$	$2.653^{+80}_{-61}$	[6,11]	4.08/6
$8^3 \times 24$	0.1395	0.1370	$0.961^{+30}_{-9}$	$3.573^{+141}_{-77}$	[7,11]	12.79/4
		0.1380	$0.917^{+24}_{-6}$	$3.411^{+122}_{-70}$	[6,11]	11.80/6
		0.1390	$0.874^{+34}_{-5}$	$3.251^{+149}_{-65}$	[6,11]	11.01/6
$8^3 \times 24$	0.1395	0.1398	$0.850^{+26}_{-9}$	$3.159^{+124}_{-69}$	[6,11]	11.17/6



TABLE X. Vector masses on  $12^3 \times 24$ , in lattice units and in units of  $r_0$ .

$L^3 \times T$	$\kappa^{\text{sea}}$	$\kappa^{\text{val}}$	$m_V a$	$m_V r_0$	Fit	$\chi^2/N_{\text{DF}}$
$12^3 \times 24$	0.1370	0.1370	$1.296^{+6}_{-4}$	$2.973^{+29}_{-31}$	[7,11]	3.85/4
		0.1380	$1.249^{+6}_{-5}$	$2.866^{+28}_{-31}$	[7,11]	4.17/4
		0.1390	$1.202^{+6}_{-5}$	$2.757^{+28}_{-30}$	[7,11]	4.77/4
		0.1395	$1.178^{+7}_{-5}$	$2.703^{+28}_{-29}$	[7,11]	5.19/4
$12^3 \times 24$	0.1380	0.1370	$1.185^{+6}_{-4}$	$3.043^{+43}_{-37}$	[7,11]	24.88/4
		0.1380	$1.135^{+7}_{-4}$	$2.915^{+43}_{-36}$	[6,11]	33.99/6
		0.1390	$1.084^{+8}_{-4}$	$2.783^{+42}_{-34}$	[6,11]	28.64/6
		0.1395	$1.058^{+9}_{-4}$	$2.717^{+42}_{-34}$	[6,11]	25.81/6
$12^3 \times 24$	0.1390	0.1370	$1.016^{+4}_{-5}$	$3.094^{+60}_{-51}$	[6,11]	6.99/6
		0.1380	$0.962^{+7}_{-3}$	$2.931^{+59}_{-48}$	[7,11]	14.24/4
		0.1390	$0.901^{+10}_{-3}$	$2.746^{+61}_{-48}$	[7,11]	8.29/4
		0.1395	$0.891^{+9}_{-1}$	$2.714^{+59}_{-47}$	[6,11]	36.73/6
$12^3 \times 24$	0.1395	0.1370	$0.930^{+9}_{-7}$	$3.195^{+54}_{-49}$	[7,11]	29.92/4
		0.1380	$0.867^{+7}_{-6}$	$2.980^{+48}_{-46}$	[6,11]	12.76/6
		0.1390	$0.814^{+8}_{-6}$	$2.796^{+48}_{-43}$	[5,11]	13.67/8
		0.1395	$0.786^{+9}_{-7}$	$2.700^{+49}_{-44}$	[5,11]	13.10/8
$12^3 \times 24$	0.1398	0.1380	$0.791^{+16}_{-11}$	$2.890^{+64}_{-20}$	[7,11]	25.71/4
		0.1390	$0.735^{+7}_{-14}$	$2.685^{+33}_{-54}$	[6,11]	14.22/6
		0.1395	$0.725^{+12}_{-16}$	$2.647^{+49}_{-62}$	[5,11]	29.11/8
		0.1398	$0.706^{+12}_{-16}$	$2.578^{+47}_{-61}$	[5,11]	25.26/8

(much lower) lattice determinations of  $m_V^2 - m_{\text{PS}}^2$  is partly due to lattice artifacts [48]. However, it is widely expected that the remaining difference, which becomes more pronounced as the valence quark mass is increased, is due to dynamical quark effects. In Fig. 12 we plot the meson hyperfine splitting  $(m_V r_0)^2 - (m_{\text{PS}} r_0)^2$  versus  $(m_{\text{PS}} r_0)^2$  for all values of  $\kappa^{\text{sea}}$ . The numerical data are compared to the  $\phi$ - $\eta_s$  splitting. Despite the relatively poor statistical accuracy, it is obvious that the numerically determined hyperfine splitting shows a trend towards the experimental point as the sea quark mass is decreased. As regards the quantification of the relative deviation from experiment between the results obtained in the quenched approximation and for finite sea quark mass, the same caveats apply as for the interpretation of Fig. 11, namely, that the comparison should be performed for fixed lattice spacing.

TABLE XI. Vector masses on  $16^3 \times 24$ , in lattice units and in units of  $r_0$ .

$L^3 \times T$	$\kappa^{\text{sea}}$	$\kappa^{\text{val}}$	$m_V a$	$m_V r_0$	Fit	$\chi^2/N_{\text{DF}}$
$16^3 \times 24$	0.1390	0.1390	$0.893^{+9}_{-6}$	$2.702^{+39}_{-28}$	[7,11]	14.64/4
		0.1395	$0.863^{+10}_{-6}$	$2.610^{+40}_{-28}$	[7,11]	14.79/4
		0.1398	$0.852^{+11}_{-6}$	$2.580^{+43}_{-27}$	[4,11]	22.82/10
$16^3 \times 24$	0.1395	0.1390	$0.813^{+8}_{-6}$	$2.801^{+43}_{-51}$	[7,11]	13.43/4
		0.1395	$0.785^{+9}_{-7}$	$2.702^{+45}_{-51}$	[7,11]	12.70/4
		0.1398	$0.773^{+10}_{-8}$	$2.664^{+46}_{-53}$	[5,11]	14.00/8
$16^3 \times 24$	0.1398	0.1390	$0.749^{+9}_{-8}$	$2.733^{+41}_{-37}$	[7,11]	2.09/4
		0.1395	$0.716^{+10}_{-8}$	$2.614^{+44}_{-37}$	[7,11]	130/4
		0.1398	$0.698^{+11}_{-10}$	$2.547^{+47}_{-41}$	[7,11]	1.60/4

TABLE XII. Nucleon masses on  $8^3 \times 24$ , in lattice units and in units of  $r_0$ .

$L^3 \times T$	$\kappa^{\text{sea}}$	$\kappa^{\text{val}}$	$m_N a$	$m_N r_0$	Fit	$\chi^2/N_{\text{DF}}$
$8^3 \times 24$	0.1370	0.1370	$2.094^{+42}_{-14}$	$4.681^{+124}_{-102}$	[6,11]	14.59/6
		0.1380	$2.020^{+43}_{-15}$	$4.517^{+124}_{-99}$	[6,11]	13.29/6
		0.1390	$1.945^{+44}_{-18}$	$4.349^{+124}_{-98}$	[6,11]	12.07/6
		0.1395	$1.907^{+49}_{-21}$	$4.264^{+132}_{-99}$	[6,11]	11.54/6
$8^3 \times 24$	0.1380	0.1370	$1.926^{+40}_{-14}$	$4.768^{+174}_{-134}$	[6,11]	11.13/6
		0.1380	$1.830^{+47}_{-10}$	$4.528^{+178}_{-125}$	[6,11]	9.43/6
		0.1390	$1.730^{+55}_{-8}$	$4.282^{+188}_{-117}$	[6,11]	7.65/6
		0.1395	$1.677^{+63}_{-7}$	$4.151^{+198}_{-114}$	[6,11]	6.74/6
$8^3 \times 24$	0.1390	0.1370	$1.687^{+29}_{-10}$	$4.877^{+132}_{-103}$	[6,11]	11.89/6
		0.1380	$1.596^{+38}_{-9}$	$4.613^{+146}_{-97}$	[6,11]	9.77/6
		0.1390	$1.511^{+44}_{-9}$	$4.368^{+155}_{-96}$	[6,11]	8.65/6
		0.1395	$1.473^{+47}_{-20}$	$4.259^{+162}_{-103}$	[6,11]	8.89/6
$8^3 \times 24$	0.1395	0.1370	$1.606^{+25}_{-22}$	$5.971^{+171}_{-141}$	[6,11]	8.73/6
		0.1380	$1.535^{+24}_{-26}$	$5.706^{+164}_{-148}$	[6,11]	7.84/6
		0.1390	$1.463^{+34}_{-20}$	$5.440^{+181}_{-209}$	[7,11]	4.81/4
		0.1395	$1.397^{+42}_{-26}$	$5.195^{+200}_{-140}$	[4,11]	9.34/10

## V. CONCLUSIONS

In this paper, we have presented the first results on the light hadron spectrum and the static quark potential obtained from dynamical simulations using an  $O(a)$  improved fermion action at  $\beta=5.2$ . Sea quark masses were chosen such that  $m_{\text{PS}}/m_V$  was in the range from 0.86 down to 0.67. The value of  $c_{\text{sw}}=1.76$  was not appropriate to remove all leading discretization effects. We wish to point out, however, that at such a low  $\beta$  value residual lattice artifacts could be rela-

TABLE XIII. Nucleon masses on  $12^3 \times 24$ , in lattice units and in units of  $r_0$ .

$L^3 \times T$	$\kappa^{\text{sea}}$	$\kappa^{\text{val}}$	$m_N a$	$m_N r_0$	Fit	$\chi^2/N_{\text{DF}}$
$12^3 \times 24$	0.1370	0.1370	$2.053^{+32}_{-22}$	$4.710^{+85}_{-69}$	[7,11]	8.29/4
		0.1380	$1.975^{+36}_{-19}$	$4.531^{+91}_{-62}$	[7,11]	7.97/4
		0.1390	$1.900^{+33}_{-10}$	$4.359^{+85}_{-50}$	[6,11]	10.42/6
		0.1395	$1.860^{+33}_{-11}$	$4.267^{+84}_{-49}$	[6,11]	9.47/6
$12^3 \times 24$	0.1380	0.1370	$1.850^{+24}_{-9}$	$4.752^{+88}_{-60}$	[7,11]	4.95/4
		0.1380	$1.763^{+23}_{-10}$	$4.528^{+85}_{-58}$	[7,11]	4.85/4
		0.1390	$1.673^{+24}_{-9}$	$4.296^{+83}_{-56}$	[7,11]	5.56/4
		0.1395	$1.626^{+24}_{-11}$	$4.176^{+83}_{-56}$	[7,11]	6.19/4
$12^3 \times 24$	0.1390	0.1370	$1.604^{+20}_{-9}$	$4.886^{+111}_{-88}$	[7,11]	15.34/4
		0.1380	$1.505^{+21}_{-10}$	$4.585^{+107}_{-83}$	[7,11]	13.01/4
		0.1390	$1.399^{+22}_{-11}$	$4.263^{+106}_{-80}$	[7,11]	10.61/4
		0.1395	$1.343^{+24}_{-11}$	$4.089^{+107}_{-77}$	[7,11]	9.33/4
$12^3 \times 24$	0.1395	0.1370	$1.434^{+19}_{-10}$	$4.927^{+95}_{-76}$	[7,11]	13.69/4
		0.1380	$1.335^{+20}_{-11}$	$4.585^{+94}_{-73}$	[7,11]	10.29/4
		0.1390	$1.233^{+20}_{-12}$	$4.234^{+92}_{-71}$	[7,11]	7.69/4
		0.1395	$1.178^{+22}_{-10}$	$4.045^{+95}_{-65}$	[6,11]	5.05/6
$12^3 \times 24$	0.1398	0.1380	$1.236^{+26}_{-15}$	$4.514^{+102}_{-63}$	[6,11]	15.02/6
		0.1390	$1.124^{+23}_{-23}$	$4.106^{+90}_{-89}$	[7,11]	14.30/4
		0.1395	$1.069^{+25}_{-20}$	$3.902^{+97}_{-76}$	[6,11]	14.69/6
		0.1398	$1.031^{+26}_{-20}$	$3.765^{+101}_{-78}$	[6,11]	14.74/6

TABLE XIV. Nucleon masses on  $16^3 \times 24$ , in lattice units and in units of  $r_0$ .

$L^3 \times T$	$\kappa^{\text{sea}}$	$\kappa^{\text{val}}$	$m_N a$	$m_N r_0$	Fit	$\chi^2/N_{\text{DF}}$
$16^3 \times 24$	0.1390	0.1390	$1.345^{+33}_{-5}$	$4.071^{+110}_{-36}$	[7,11]	5.49/4
		0.1395	$1.295^{+32}_{-6}$	$3.918^{+106}_{-36}$	[7,11]	6.24/4
		0.1398	$1.264^{+31}_{-7}$	$3.826^{+102}_{-37}$	[7,11]	6.72/4
$16^3 \times 24$	0.1395	0.1390	$1.261^{+25}_{-10}$	$4.344^{+99}_{-80}$	[7,11]	13.78/4
		0.1395	$1.205^{+24}_{-11}$	$4.149^{+96}_{-79}$	[7,11]	10.92/4
		0.1398	$1.164^{+24}_{-19}$	$4.010^{+96}_{-92}$	[7,11]	9.08/4
$16^3 \times 24$	0.1398	0.1390	$1.144^{+36}_{-31}$	$4.178^{+136}_{-117}$	[7,11]	23.51/4
		0.1395	$1.065^{+47}_{-35}$	$3.888^{+173}_{-133}$	[7,11]	19.78/4
		0.1398	$1.030^{+43}_{-34}$	$3.762^{+160}_{-127}$	[7,11]	17.48/4

tively large, even after full  $O(a)$  improvement. This question clearly requires further investigation.

We have addressed the important issue of finite-size effects, which are expected to be larger in dynamical simulations, compared to the quenched approximation. By simulating three different lattice sizes for a range of sea quark masses, we found that finite-size effects are practically absent for box sizes  $L \gtrsim 1.6$  fm and sea quark masses which give  $m_{\text{PS}}/m_V \gtrsim 0.67$ . This is observed in the data for the static quark potential and hadron masses. However, for lighter dynamical quarks one would expect that yet larger volumes are required.

Instead of presenting quantitative results for the light hadron spectrum, we have concentrated on highlighting the effects of dynamical quarks. Although the evidence for string breaking in the data for the static quark potential and for an improved behavior of the parameter  $J$  remains inconclusive, we have detected significant effects due to dynamical quarks. Namely, the Coulombic part of the static quark potential is enhanced for finite sea quark mass, and the vector-pseudoscalar hyperfine splitting moves closer to the experi-

TABLE XV.  $\Delta$  masses on  $8^3 \times 24$ , in lattice units and in units of  $r_0$ .

$L^3 \times T$	$\kappa^{\text{sea}}$	$\kappa^{\text{val}}$	$m_\Delta a$	$m_\Delta r_0$	Fit	$\chi^2/N_{\text{DF}}$
$8^3 \times 24$	0.1370	0.1370	$2.146^{+39}_{-13}$	$4.799^{+121}_{-103}$	[7,11]	5.73/4
		0.1380	$2.070^{+40}_{-14}$	$4.629^{+120}_{-100}$	[7,11]	4.79/4
		0.1390	$1.989^{+44}_{-13}$	$4.448^{+125}_{-96}$	[7,11]	4.64/4
		0.1395	$1.947^{+46}_{-12}$	$4.353^{+128}_{-94}$	[7,11]	4.75/4
$8^3 \times 24$	0.1380	0.1370	$2.131^{+51}_{-1}$	$5.274^{+202}_{-143}$	[6,11]	16.72/6
		0.1380	$1.918^{+37}_{-4}$	$4.747^{+169}_{-129}$	[7,11]	6.51/4
		0.1390	$1.854^{+34}_{-8}$	$4.588^{+160}_{-126}$	[7,11]	3.99/4
		0.1395	$1.831^{+33}_{-12}$	$4.531^{+158}_{-126}$	[7,11]	3.93/4
$8^3 \times 24$	0.1390	0.1370	$1.790^{+34}_{-9}$	$5.174^{+145}_{-107}$	[6,11]	17.07/6
		0.1380	$1.717^{+32}_{-8}$	$4.964^{+139}_{-102}$	[6,11]	14.01/6
		0.1390	$1.651^{+27}_{-9}$	$4.773^{+127}_{-100}$	[6,11]	11.26/6
		0.1395	$1.621^{+27}_{-13}$	$4.687^{+124}_{-101}$	[6,11]	10.62/6
$8^3 \times 24$	0.1395	0.1370	$1.718^{+42}_{-6}$	$6.389^{+219}_{-126}$	[6,11]	10.07/6
		0.1380	$1.644^{+42}_{-6}$	$6.111^{+214}_{-121}$	[6,11]	9.26/6
		0.1390	$1.578^{+38}_{-13}$	$5.866^{+200}_{-124}$	[6,11]	10.38/6
		0.1395	$1.538^{+43}_{-19}$	$5.718^{+210}_{-130}$	[7,11]	7.59/4

TABLE XVI.  $\Delta$  masses on  $12^3 \times 24$ , in lattice units and in units of  $r_0$ .

$L^3 \times T$	$\kappa^{\text{sea}}$	$\kappa^{\text{val}}$	$m_\Delta a$	$m_\Delta r_0$	Fit	$\chi^2/N_{\text{DF}}$
$12^3 \times 24$	0.1370	0.1370	$2.139^{+29}_{-1}$	$4.907^{+79}_{-49}$	[7,11]	10.07/4
		0.1380	$2.071^{+27}_{-3}$	$4.750^{+75}_{-48}$	[7,11]	10.48/4
		0.1390	$2.000^{+25}_{-4}$	$4.587^{+70}_{-47}$	[7,11]	10.97/4
		0.1395	$1.966^{+23}_{-5}$	$4.511^{+65}_{-47}$	[7,11]	11.01/4
$12^3 \times 24$	0.1380	0.1370	$1.933^{+30}_{-2}$	$4.963^{+101}_{-58}$	[7,11]	8.07/4
		0.1380	$1.855^{+30}_{-2}$	$4.763^{+99}_{-56}$	[7,11]	6.26/4
		0.1390	$1.773^{+32}_{-2}$	$4.553^{+102}_{-53}$	[7,11]	5.89/4
		0.1395	$1.754^{+22}_{-5}$	$4.504^{+82}_{-64}$	[7,11]	5.19/4
$12^3 \times 24$	0.1390	0.1370	$1.714^{+31}_{-6}$	$5.221^{+136}_{-90}$	[7,11]	18.87/4
		0.1380	$1.630^{+30}_{-6}$	$4.964^{+131}_{-87}$	[7,11]	16.59/4
		0.1390	$1.545^{+27}_{-6}$	$4.707^{+123}_{-83}$	[7,11]	13.88/4
		0.1395	$1.502^{+29}_{-6}$	$4.576^{+124}_{-80}$	[7,11]	12.39/4
$12^3 \times 24$	0.1395	0.1370	$1.539^{+26}_{-10}$	$5.285^{+115}_{-80}$	[7,11]	26.22/4
		0.1380	$1.457^{+20}_{-16}$	$5.005^{+97}_{-87}$	[7,11]	21.69/4
		0.1390	$1.372^{+19}_{-19}$	$4.711^{+92}_{-91}$	[7,11]	17.49/4
		0.1395	$1.329^{+22}_{-20}$	$4.565^{+99}_{-93}$	[7,11]	15.43/4
$12^3 \times 24$	0.1398	0.1380	$1.373^{+34}_{-21}$	$5.016^{+129}_{-83}$	[7,11]	34.34/4
		0.1390	$1.273^{+32}_{-26}$	$4.648^{+121}_{-99}$	[7,11]	27.18/4
		0.1395	$1.222^{+32}_{-27}$	$4.463^{+121}_{-103}$	[7,11]	23.00/4
		0.1398	$1.191^{+29}_{-28}$	$4.349^{+113}_{-105}$	[7,11]	20.55/4

mental value as the sea quark mass is decreased. Furthermore, pairs of  $(m_V r_0, (m_{\text{PS}} r_0)^2)$  show a trend towards experiment when dynamical quarks are “switched on.”

The results presented here serve as a guideline for ongoing investigations, which are performed using the fully  $O(a)$  improved action for two flavors of dynamical quarks, whose masses are closer to the chiral limit than those used in this study.

## ACKNOWLEDGMENTS

We are grateful to the ALPHA Collaboration for communicating to us their preliminary value for the improvement coefficient at  $\beta=5.2$ . We acknowledge the support of the Particle Physics and Astronomy Research Council under grant GR/L22744. H.W. acknowledges the financial support of PPARC.

TABLE XVII.  $\Delta$  masses on  $16^3 \times 24$ , in lattice units and in units of  $r_0$ .

$L^3 \times T$	$\kappa^{\text{sea}}$	$\kappa^{\text{val}}$	$m_\Delta a$	$m_\Delta r_0$	Fit	$\chi^2/N_{\text{DF}}$
$16^3 \times 24$	0.1390	0.1390	$1.599^{+34}_{-20}$	$4.838^{+116}_{-73}$	[6,11]	32.43/6
		0.1395	$1.555^{+34}_{-19}$	$4.704^{+114}_{-68}$	[6,11]	28.16/6
		0.1398	$1.532^{+35}_{-19}$	$4.635^{+115}_{-69}$	[6,11]	25.28/6
$16^3 \times 24$	0.1395	0.1390	$1.395^{+28}_{-5}$	$4.805^{+111}_{-81}$	[7,11]	11.43/4
		0.1395	$1.347^{+30}_{-6}$	$4.640^{+115}_{-79}$	[7,11]	10.63/4
		0.1398	$1.318^{+30}_{-8}$	$4.538^{+116}_{-80}$	[7,11]	10.20/4
$16^3 \times 24$	0.1398	0.1390	$1.296^{+29}_{-11}$	$4.733^{+112}_{-55}$	[7,11]	19.39/4
		0.1395	$1.244^{+27}_{-11}$	$4.541^{+106}_{-56}$	[7,11]	17.22/4
		0.1398	$1.208^{+29}_{-12}$	$4.411^{+111}_{-56}$	[7,11]	15.52/4

## APPENDIX

In Tables VI–XVII we list the meson and baryon masses for all combinations of  $\kappa^{\text{sea}}$  and  $\kappa^{\text{val}}$ , and on all lattice sizes used in the simulations.

In the following tables we also list the fitting interval and the value of  $\chi^2/N_{\text{DF}}$ , obtained from a correlated fit to Eq. (32) or (33), respectively. Some of the fits produce values of  $\chi^2/N_{\text{DF}}$  which would normally be regarded as unacceptably large, even though we are confident that the fit intervals were

properly tuned. In such cases we have compared the results for the masses to those obtained using an uncorrelated fit over the same interval. We always found that the uncorrelated fit gave results which, within errors, were perfectly compatible with those from the correlated fit, while producing values for  $\chi^2/N_{\text{DF}}$  which were significantly below 1. Thus we are confident that the results presented in Tables VI–XVII below are reliable and that a double exponential is an appropriate model function in all cases, but that correlations in the data are clearly present.

- 
- [1] T. Yoshié, Nucl. Phys. B (Proc. Suppl.) **63**, 3 (1998).
  - [2] S. Güsken, Nucl. Phys. B (Proc. Suppl.) **63**, 16 (1998).
  - [3] S. Gottlieb, Nucl. Phys. B (Proc. Suppl.) **53**, 155 (1997).
  - [4] K. Jansen, Nucl. Phys. B (Proc. Suppl.) **53**, 127 (1997).
  - [5] SESAM Collaboration, U. Glässner *et al.*, Phys. Lett. B **383**, 98 (1996).
  - [6] SESAM Collaboration, N. Eicker *et al.*, Phys. Lett. B **407**, 290 (1997).
  - [7] SESAM Collaboration, N. Eicker *et al.*, Phys. Rev. D **59**, 014509 (1999).
  - [8] R. D. Mawhinney, Nucl. Phys. B (Proc. Suppl.) **60A**, 306 (1998).
  - [9] CP-PACS Collaboration, S. Aoki *et al.*, Nucl. Phys. B (Proc. Suppl.) **60A**, 335 (1998); CP-PACS Collaboration, S. Aoki *et al.*, *ibid.* **63**, 161 (1998); **63**, 221 (1998).
  - [10] MILC Collaboration, C. Bernard *et al.*, Nucl. Phys. B (Proc. Suppl.) **60A**, 297 (1998); MILC Collaboration, C. Bernard *et al.*, *ibid.* **63**, 215 (1998).
  - [11] SESAM and  $T\chi L$  Collaborations, T. Lippert *et al.*, Nucl. Phys. B (Proc. Suppl.) **60A**, 311 (1998); SESAM and  $T\chi L$  Collaborations, H. Hoerber *et al.*, *ibid.* **63**, 218 (1998); SESAM and  $T\chi L$  Collaborations, G. S. Bali *et al.*, *ibid.* **63**, 209 (1998).
  - [12] UKQCD Collaboration, M. Talevi, Nucl. Phys. B (Proc. Suppl.) **63**, 227 (1998).
  - [13] K. Jansen *et al.*, Phys. Lett. B **372**, 275 (1996).
  - [14] M. Lüscher, S. Sint, R. Sommer, and P. Weisz, Nucl. Phys. **B478**, 365 (1996).
  - [15] M. Lüscher, S. Sint, R. Sommer, P. Weisz, and U. Wolff, Nucl. Phys. **B491**, 323 (1997).
  - [16] R. G. Edwards, U. M. Heller, and T. R. Klassen, Nucl. Phys. B (Proc. Suppl.) **63**, 847 (1998).
  - [17] K. Jansen and R. Sommer, Nucl. Phys. **B530**, 185 (1998).
  - [18] UKQCD Collaboration (in preparation).
  - [19] A. M. Horowitz, Phys. Lett. B **195**, 216 (1987); Nucl. Phys. **B280**, 510 (1987); Phys. Lett. B **268**, 247 (1991); A. D. Kennedy, R. Edwards, H. Mino, and B. Pendleton, Nucl. Phys. B (Proc. Suppl.) **47**, 781 (1996).
  - [20] B. Sheikholeslami and R. Wohlert, Nucl. Phys. **B259**, 572 (1985).
  - [21] H. van der Vorst, SIAM (Soc. Ind. Appl. Math.) J. Sci. Stat. Comput. **12**, 631 (1992); A. Frommer *et al.*, Int. J. Mod. Phys. C **5**, 1073 (1994).
  - [22] UKQCD Collaboration, Z. Sroczynski, S. M. Pickles, and S. P. Booth, Nucl. Phys. B (Proc. Suppl.) **63**, 949 (1998).
  - [23] J. C. Sexton and D. H. Weingarten, Nucl. Phys. **B380**, 665 (1992).
  - [24] M. Creutz and A. Goksch, Phys. Rev. Lett. **63**, 9 (1989).
  - [25] R. M. McLachlan and P. Atela, Nonlinearity **5**, 541 (1992).
  - [26] UKQCD Collaboration, P. Lacey *et al.*, Phys. Rev. D **51**, 6403 (1995).
  - [27] UKQCD Collaboration, C. R. Allton *et al.*, Phys. Rev. D **49**, 474 (1994).
  - [28] P. J. Brockwell and R. A. Davis, *Time Series: Theory and Methods* (Springer-Verlag, Berlin, 1987).
  - [29] R. Sommer, Nucl. Phys. **B411**, 839 (1994).
  - [30] M. Albanese *et al.*, Phys. Lett. B **192**, 163 (1987).
  - [31] S. Perantonis, A. Huntley, and C. Michael, Nucl. Phys. **B326**, 544 (1989).
  - [32] UKQCD Collaboration, H. Wittig, Nucl. Phys. B (Proc. Suppl.) **42**, 288 (1995).
  - [33] C. Michael, Nucl. Phys. **B259**, 58 (1985).
  - [34] M. Lüscher and U. Wolff, Nucl. Phys. **B339**, 222 (1990).
  - [35] R. G. Edwards, U. M. Heller, and T. R. Klassen, Nucl. Phys. **B517**, 377 (1998).
  - [36] M. Guagnelli, R. Sommer, and H. Wittig, Nucl. Phys. **B535**, 389 (1998).
  - [37] M. Lüscher, Nucl. Phys. **B180**, 317 (1981).
  - [38] UKQCD Collaboration, C. Michael and J. Peisa, Phys. Rev. D **58**, 034506 (1998).
  - [39] C. Michael, Nucl. Phys. B (Proc. Suppl.) **26**, 417 (1992).
  - [40] O. Philipsen and H. Wittig, Phys. Rev. Lett. **81**, 4056 (1998); F. Knechtli and R. Sommer, Phys. Lett. B **440**, 345 (1998).
  - [41] C. Michael, Phys. Rev. D **49**, 2616 (1994); C. Michael and A. McKerrell, *ibid.* **51**, 3745 (1995).
  - [42] P. A. Rowland, Ph.D. thesis, University of Edinburgh, 1997; UKQCD Collaboration, “Quenched light hadron spectrum using non-perturbative  $O(a)$  improvement” (in preparation).
  - [43] S. Sint and P. Weisz, Nucl. Phys. **B502**, 251 (1997).
  - [44] UKQCD Collaboration, P. Lacey and C. Michael, Phys. Rev. D **52**, 5213 (1995).
  - [45] C. Allton *et al.*, Nucl. Phys. **B489**, 427 (1997).
  - [46] UKQCD Collaboration, H. P. Shanahan *et al.*, Phys. Rev. D **55**, 1548 (1997).
  - [47] UKQCD Collaboration, A. C. Irving *et al.*, Phys. Rev. D **58**, 114504 (1998).
  - [48] UKQCD Collaboration, C. R. Allton *et al.*, Phys. Lett. B **284**, 377 (1992); M. Göckeler *et al.*, Phys. Rev. D **57**, 5562 (1998); H. Wittig, Nucl. Phys. B (Proc. Suppl.) **63**, 47 (1998).